

The structure of the nuclear stellar cluster of the Milky Way

R. Schödel¹, A. Eckart¹, T. Alexander^{4,5}, D. Merritt⁶, R. Genzel^{2,3}, A. Sternberg⁷, L. Meyer¹, F. Kul¹, J. Moutaka⁸, T. Ott², and C. Straubmeier¹

¹ I. Physikalisches Institut, Universität zu Köln, Zùlpicher Str. 77, 50937 Köln, Germany

e-mail: rainer.eckart, leo.kul, cstraubm@ph1.uni-koeln.de

² Max-Planck-Institut für extraterrestrische Physik, Giessenbachstraße, 85748 Garching, Germany

e-mail: genzel, ott@mpe.mpg.de

³ Also: Department of Physics, University of California, Berkeley, CA 94720, USA

⁴ Faculty of Physics, Weizmann Institute of Science, 76100 Rehovot, Israel

e-mail: tal.alexander@weizmann.ac.il

⁵ Incumbent of the William Z. & Eda Bess Novick career development chair

⁶ Department of Physics, Rochester Institute of Technology, 54 Lomb Memorial Drive, Rochester, NY 14623-5604

e-mail: merritt@astro.rit.edu

⁷ School of Physics and Astronomy and the Wise Observatory, The Beverly and Raymond Sackler Faculty of Exact Sciences, Tel Aviv University, Tel Aviv 69978, Israel

e-mail: amiel@wise.tau.ac.il

⁸ Laboratoire d'Astrophysique de Toulouse, UMR 5572, Observatoire Midi-Pyrénées, 14 avenue Edouard Belin, 31400 Toulouse, France

e-mail: jihane.moutaka@ast.obs-mip.fr

ABSTRACT

Aims. The centre of the Milky Way is the nearest nucleus of a galaxy and offers a unique possibility to study the structure and dynamics of a dense stellar cluster around a super-massive black hole.

Methods. We present high-resolution seeing limited and AO NIR imaging observations of the stellar cluster within about one parsec of Sgr A*, the massive black hole at the centre of the Milky Way. Stellar number counts and the diffuse background light density were extracted from these observations in order to examine the structure of the nuclear stellar cluster. A detailed map of the variation of interstellar extinction in the central ~ 0.5 pc of the Milky Way is presented and used to correct the stellar number counts and diffuse light density.

Results. Our findings are as follows: (a) A broken-power law provides an excellent fit to the overall structure of the GC nuclear cluster. The power-law slope of the cusp is $\Gamma = 0.19 \pm 0.05$, the break radius is $R_{\text{break}} = 6.0'' \pm 1.0''$ or 0.22 ± 0.04 pc, and the cluster density decreases with a power-law index of $\Gamma = 0.75 \pm 0.1$ outside of R_{break} . (b) Using the best velocity dispersion measurements from the literature, we derive higher mass estimates for the central parsec than assumed until now. The inferred density of the cluster at the break radius is $2.8 \pm 1.3 \times 10^6 M_{\odot} \text{pc}^{-3}$. This high density agrees well with the small extent and flat slope of the cusp. Possibly, the mass of the stars makes up only about 50% of the total cluster mass. (c) Possible indications of mass segregation in the cusp are found. (d) The cluster appears not entirely homogeneous. Several density clumps are detected that are concentrated at projected distances of $R = 3''$ and $R = 7''$ from Sgr A*. (e) There appears to exist an under-density of horizontal branch/red clump stars near $R = 5''$, or an over-density of stars of similar brightness at $R = 3''$ and $R = 7''$. (f) The extinction map in combination with cometary-like features in an L'-band image may provide support for the assumption of an outflow from Sgr A*.

Key words. Stellar dynamics – Galaxy: centre –

1. Introduction

The centre of the Milky Way is the closest galactic nucleus, located at a distance of about 8 kpc (Reid 1993; Eisenhauer et al. 2003). It represents the only case where it is possible to observe and analyse the interplay between a central massive black hole (e.g., Eckart & Genzel 1996; Genzel et al. 2000; Ghez et al. 2000; Schödel et al. 2002; Ghez et al. 2003) and the gas and stars in its environment directly through observation of individual stellar sources and gas features. A particular point of interest is the density structure of the nuclear star cluster. From theoretical considerations one expects to observe a stellar cusp around the black hole.

The way in which a central black hole alters the structure of a surrounding cluster has been examined theoretically starting from two fundamentally different assumptions: On the one hand, there are adiabatic models, in which the growth rate of the black hole is long compared to the dynamical time scale of the cluster, but short with respect to the two-body relaxation time of the cluster. Under these assumptions, a $r^{-3/2}$ -cusp will develop in a spherically symmetric, non-rotating system that is initially isothermal (Young 1980). In the case of rotating systems and non-isothermal clusters, cusps as steep as $r^{-5/2}$ may develop (Lee & Goodman 1989; Quinlan et al. 1995). On the other hand, the system may be older than the two-body relaxation time. Bahcall & Wolf (1976) found that in this case, the final configuration will be a $r^{-7/4}$ -cusp for a single-mass stellar population, independent of the initial

conditions. Bahcall & Wolf (1977) extended their work to a system containing stars of two different masses and found that the steady-state distribution near the black hole approaches a power-law with index:

$$\gamma = \frac{m_1}{4m_2} + \frac{3}{2}, m_1 \leq m_2. \quad (1)$$

Therefore, in a stellar cluster with a range of stellar masses, one would expect a slope with γ in the range $3/2$ to $7/4$ (From here on, we will use γ as notation for the power-law index of the space density and Γ for the power-law index of the projected stellar density, the quantity that is actually observed). Murphy et al. (1991) simulated the evolution of multi-mass clusters with a Fokker-Planck code. They also found that the slope of the final cusp will lie in the range $-7/4$ to $-1/2$ (see also Lightman & Shapiro 1977). The latter value represents the case of high-density nuclei, where stellar collisions become important and lead to a flattening of the cusp.

Hence, a stellar cusp is expected to be the signature of a central black hole embedded in a stellar cluster. The properties of the cusp, particularly the index of the power-law that describes the stellar density, should reflect the formation history of the system.

Unfortunately, only the structure of the light distribution can be examined in external galaxies because of the lack of sensitivity and resolution of the current generation of instruments. Surface brightness measurements, however, may be dominated by the light from a few extremely bright stars and may therefore be only of limited use when examining the structure of nuclear clusters. Due to its proximity, the GC nuclear cluster can be resolved into individual sources and may represent therefore an ideal test case for cusp theories.

In one of the early attempts to determine the density structure of the stellar cluster around the GC, Catchpole et al. (1990) counted giant stars in a $1^\circ \times 2^\circ$ region centred on the GC. They found that the increase of the stellar volume density toward the centre was about $\propto r^{-2}$, as in an isothermal cluster, where r is the distance to the GC. Haller et al. (1996) determined the surface brightness profile at distances between $15''$ and $200''$ from Sgr A* and found a dependence $\propto R^{-0.8}$, where R denotes the projected distance from the centre of the cluster (see also Becklin & Neugebauer 1968). This corresponds to a density distribution $\propto r^{-1.8}$.

Eckart et al. (1993) and Genzel et al. (1996) presented number density counts from high-resolution near-infrared (NIR) speckle imaging observations at the diffraction limit of a 4 m-class telescope in a region from about $1''$ to $20''$. They found that the stellar density appears to be described well by an isothermal cluster ($\rho \propto r^{-2}$). In the inner few arc-seconds the surface density distribution was found to flatten. The core radius of the cluster was determined to $\sim 0.15 - 0.4$ pc (Eckart et al. 1993; Genzel et al. 1996). Some indication for a cusp, i.e. a central density excess above the flat core of an isothermal cluster was found in follow-up work (e.g., Eckart et al. 1995; Alexander 1999), but the evidence remained somewhat inconclusive. At this point, all attempts to determine the structure of the GC nuclear cluster were limited to stars brighter than $\text{mag}_K = 15$ and to resolutions of a few $0.1''$ (with the exception of the speckle imaging).

This situation changed with the commissioning of the adaptive optics (AO) module NAOS and the NIR camera CONICA (the combination of which is abbreviated NACO) at the ESO 8 m-class VLT unit telescope 4 on Paranal, Chile. The Paranal mountain is an ideal site for observations of the GC, which passes close to zenith at this location. Additionally, the unique NIR wavefront sensor of NAOS allows to lock the AO on the NIR bright supergiant IRS 7 that is located just $\sim 6''$ from Sgr A*. With this instrument, imaging observations can be obtained with a resolution of the order 50 milli-arc-seconds (mas) that are about 2-3 magnitudes deeper than previous speckle imaging observations. Genzel et al. (2003b) used the first NACO H- and K-band imaging data to present a new analysis of the stellar number density in the GC. They combined high-resolution number counts from NACO data in the region from $0.1''$ to $10''$ projected radius from Sgr A* with lower resolution number counts from speckle imaging observations of fields at distances between $10''$ and $100''$. The combined surface density counts vs. distance from Sgr A* showed that the counts could be described reasonably well by an isothermal cluster at distances greater than $5 - 10''$. They could show, for the first time, clear evidence for a density excess above a flat core within $\sim 2''$ of Sgr A*. By fitting a broken power-law to the number density counts a power law index of $\gamma = -1.4 \pm 0.1$ was determined for the stellar space density distribution in the cusp. However, they also find that a large number of the stars with $\text{mag}_K \leq 15$ inside a projected radius of $10''$ appear to be of early type. The presence of these massive, young stars indicates that the visible part of the GC cluster may not be dominated by a stellar population that is old and had time to settle into a relaxed state as is assumed in many cusp formation theories. It seems that at least among the stars brighter than $\text{mag}_K = 15$ a significant fraction belongs to the discs of young, massive stars discovered in the inner few arc seconds around Sgr A* (e.g., see Paumard et al. 2006). Scoville et al. (2003) find a flatter brightness profile than Genzel et al. (2003b) from analysing the surface brightness in HST images. Clearly, the question on which is the best technique to measure the structure of the GC stellar cluster – surface brightness measurements or number counts – must be addressed.

The present work builds up on and expands the work of Genzel et al. (2003b). The differences/new techniques are in particular: a) Use of a new, homogeneous data set. All high-resolution imaging data in this work are from AO observations with NACO/VLT¹ in the K-band. They are considerably less affected by saturation than the data in our previous work and reach out to a projected radius of about $20''$, well beyond the extent of the cusp (the AO data in Genzel et al. 2003b, reached only out to $10''$). We do not need to combine star counts from different sources. b) High-quality seeing limited images are combined with the AO imaging data. They provide independent estimates of star counts and of the background light density, which cannot be determined reasonable in the AO images. c) PSF fitting with a spatially variable PSF is applied to optimise the detection of stellar sources. d) The diffuse background light is analysed in order to determine the structure of the faint, unresolved stellar component of the cluster. e) Various methods are used to extract the shape of the underlying cluster from the star counts. Binning of the star counts is avoided. Non-parametric methods are applied to derive the surface and space density of the cluster. We address f) the problem of surface brightness vs. star counts. g) The star counts and background light density analyses are corrected for extinction. h) Besides focusing only on the radially averaged large scale structure of the cluster, the two-dimensional structure of the cluster is examined as well. Significant inhomogeneities of the cluster are detected at several locations. i) The surface density of stars is derived for different

¹ Based on observations collected at the European Southern Observatory, Chile, programs 073.B-0745 and 075.C-0138.

stellar magnitude ranges, which makes it possible to search for effects of mass segregation and to probe the old, most probably dynamically relaxed stellar population that is represented by horizontal branch/red clump stars.

Throughout the paper we will adopt a GC distance of 7.6 kpc (Eisenhauer et al. 2005). At this distance, one arc second corresponds to 0.037 pc.

2. Observations and data reduction

2.1. ISAAC imaging

The GC was observed with the NIR camera and spectrometer ISAAC at the ESO VLT unit telescope 4 on Paranal on 2 July 1999 and on 27 July 2005. Filters used were a narrow band filter of $0.02\,\mu\text{m}$ width centred at $2.09\,\mu\text{m}$ and the J-band filter in 1999, the H-band filter in 2005. Details of the observations are given in Tab. 1.

The data were sky subtracted and corrected for bad pixels. Figure 1 shows a colour image composed of the ISAAC J and K observations (which have both a similar PSF FWHM, while the FWHM due to seeing in the H-band observations was about twice as large). The colour image illustrates the strong, patchy and highly variable extinction in the GC. It shows also that there is a general minimum of the extinction on the central cluster and in a band running north-east to south-west across it, as described by Scoville et al. (2003).

2.2. AO imaging data

The field-of-view (FOV) of the AO observations is marked with a white square in Fig. 1.

Various sets of data were chosen for the analysis of the stellar number density and the interstellar extinction in the central parsec. The data were selected according to criteria such as seeing, size of the isoplanatic angle, quality of AO correction, coverage of a large FOV, and the central filter wavelength. A summary of all data can be found in Tab. 2.

When imaging the field centred on Sgr A*, the NIR wavefront sensor of NAOS was locked on the bright supergiant IRS 7, located about $6''$ north of Sgr A*. Mosaic imaging was applied by using a rectangular dither pattern in order to enlarge the FOV. Several dithered exposures of a dark cloud near the GC ($713''$ west, $400''$ north of Sgr A*), a region largely devoid of stars, were interspersed with all observations in order to sample the sky background.

In all cases, the images were sky subtracted, flat-fielded, and corrected for dead/bad pixels during data reduction. After shifting the dithered images to a common position, they were median combined to obtain a final mosaic. In Fig. 2 we show the sum image of the $2.27\,\mu\text{m}$ and $2.30\,\mu\text{m}$ intermediate band (IB) filter data of the central field.

3. Structure of the cluster

3.1. Seeing limited observations

The IDL program package *StarFinder* (Diolaiti et al. 2000) was used for source detection, photometry, and background estimation. Photometric calibration was based on stellar magnitudes given by Ott et al. (1999, K-band: IRS 16NE, IRS 33N, IRS 33SW, ID 62, ID 96) and Blum et al. (1996, H-band: IRS 16NE, IRS 33N, IRS 33SW). Selection criteria for these stars were that the calibration stars should be isolated and bright, but not variable.

3.1.1. Extinction

When examining the structure of the central stellar cluster, it is desirable to take interstellar extinction into account. For the ISAAC images, a simple approach was taken by assuming that all stars in the FOV have the same intrinsic colour of $H - K = 0.15$.

How well justified is the assumption of a single intrinsic stellar colour? The intrinsic $H - K$ colours of normal stars span a small range in magnitude. More than 94% of the stars in our seeing-limited sample have $\text{mag}_K > 12$. They are therefore either giants or main sequence stars. Main sequence stars in the considered magnitude range must be of class O or B. Such stars are only observed in significant numbers in the innermost arcsecond near Sgr A* (Eisenhauer et al. 2005; Paumard et al. 2006). Assuming that all stars are early K giants will therefore introduce an uncertainty < 0.1 mag in the measured colour for more than 90% of the stars.

Median stellar colours for the ISAAC images were obtained from the measured individual stellar colours by taking the median of the 25 nearest stars at each position in the image. In this way, the effect of any possible individual erroneous measurements was minimised. Extinction values were then derived from the colours by applying the Draine extinction law, $A_\lambda \propto \lambda^{-1.75}$ (Draine 1989). The consequence of this procedure is that the resolution of the obtained extinction map ranges between $\sim 2.5''$ in the densest parts of the cluster, near Sgr A*, to $\sim 10''$ near the edge of the image. The spatial resolution decreases down to $\sim 15''$ in the southwestern corner, where few stars were detected due to the presence of a large dark cloud. The statistical uncertainty of the derived extinction values is ≤ 0.2 mag in more than 90% of the map and never higher than 0.3 mag. The systematic error of the extinction map depends on the uncertainty of the absolute calibration. An error in the absolute calibration will have no influence on the determined *shape* of the stellar cluster because it will only shift the counts/light densities by a fixed factor. The absolute calibration was chosen such that $A_K \approx 2.8$ near Sgr A* (Eisenhauer et al. 2005).

The map of the interstellar extinction derived in this way is shown in the left panel of Fig. 3. The right panel shows the extinction contours overlaid onto the combined J+K false colour image. It can be seen that darker regions and regions of low stellar density correlate well with regions of increased extinction. This test by eye confirms the general validity of the approach. However, each method to measure extinction has its drawbacks. A general limitation, certainly applicable in this case, is that one sees only the

projection of the target on the sky and lacks three-dimensional information. In regions where the extinction is so high that almost only foreground stars are detected, e.g. the southwestern region, extinction will therefore be underestimated significantly. However, we do not include the problematic regions in our analysis, which is limited to projected distances $R \leq 60''$ from Sgr A*.

The extinction map presented here compares favourably with the map presented by Scoville et al. (2003). Very similar features can be found, such as a general minimum of the extinction in a strip southwest-northeast across the center and increased extinction in the area of the circum-nuclear disc. Even details, like the linear southeast-northwest running feature at about $(10'', -15'')$, with a lower extinction area to the northeast, agree well.

From the extinction map, we derived maps for the correction of stellar counts and background light density. While this correction is straightforward for the light density, assumptions on the luminosity function must be made in order to correct the star counts. Hence, the counts at a given location were multiplied with a correction factor that was derived by assuming a power law index of the stellar luminosity function of $\beta = 0.23$, derived from the KLF (see section 3.2.4 and Fig. 10).

3.1.2. Star counts beyond 0.5 pc

The analysis of the star counts was done on the $2.09\mu\text{m}$ image because of the low extinction in this band and because of the high resolution. Seeing was excellent ($\sim 0.4''$) and stable during the $2.09\mu\text{m}$ observations. Contrary to observations with adaptive optics, seeing limited observations do not suffer from PSF variations due to the isoplanatic angle. Therefore it is possible to extract a PSF that is valid for the entire FOV. More than 20,000 stars were detected in the FOV of the ISAAC $2.09\mu\text{m}$ observations. We limited our analysis to a region within $\sim 60''$ of Sgr A* in order to be able to extract counts in full rings around the centre (the FOV is not centred on Sgr A*, see Fig. 1) and in order to avoid the region of extremely high extinction to the southwest of Sgr A*, for which the extinction could not be accurately measured (see Fig. 3). The completeness of the star counts was determined via the technique of introducing artificial stars into the image and trying to re-detect them. The image was probed on a dense grid of $\sim 0.74'' \times 0.74''$. In order to avoid artificially increasing the crowding, the procedure of introducing and recovering artificial stars was repeated various times with a sufficiently large grid (meaning the distance between artificial point sources was greater than several times the PSF FWHM) that was shifted with each try. Table 3 lists the completeness levels of the ISAAC $2.09\mu\text{m}$ image for the entire inner $60''$, for the inner $15''$ and for a ring $15'' < R < 60''$. The central region is highly incomplete. Therefore the analysis of the star counts in the seeing limited data was limited to $\text{mag}_K \leq 16$ and $R > 15''$.

In order to obtain the stellar number density, the stars were counted in rings of variable width around Sgr A*. Since the stellar density decreases from Sgr A*, it is desirable to vary the binning radius in order to give each data point roughly the same statistical weight. The radius of a circle that contained a given number of stars (in this case 25) was determined for each pixel in the image. The azimuthal average of this smoothing radius at each projected distance was then used as the width of the rings around Sgr A* in which the stellar density was measured. The completeness and extinction corrected stellar density for $\text{mag}_K \leq 16$ and $15'' < R < 60''$ obtained in this way is shown in Fig. 4. The uncertainties were calculated from the uncertainties of the completeness correction, the masked area, and of the extinction correction. Error bars on the x-axis were estimated from the standard deviation of the stars within a given ring from the mean radius of the ring. For the extinction corrected data we added the uncertainty of the radial location of the extinction value (because of the limited resolution of the extinction map) quadratically to the uncertainty of the error bars.

An excellent fit is provided by a power-law with an index $\Gamma = 0.68 \pm 0.02$, where the uncertainty is the formal fit error. If the data are not corrected for extinction, the resulting power-law index is $\Gamma = 0.57 \pm 0.01$.

3.1.3. The background light density

Star counts on the ISAAC images have the limitation that the crowding in the field is high and that the spatial resolution of the data is limited by seeing. Due to the masking of regions of high incompleteness, the analysis could not be extended to the central $15''$. Also, it was limited to stars $\text{mag}_K \leq 16$. In order to further constrain the structure of the faint, unresolved stellar population, we analysed the background light density. Such a study was pioneered by Philipp et al. (1999) on the inner 30 pc of the bulge, but with a spatial resolution that was a factor ~ 2 lower than in the present work.

StarFinder extracts point sources by PSF fitting, calculates a smooth background, and provides images of the detected point sources, of the background, and of the residuum. For background estimation, the image is partitioned into rectangular sub-frames. The sky background value computed for these sub-frames (via the IDL library routine SKY that is based on a DAOPHOT routine of the same name) is assigned to grid points corresponding to the centres of the frames. A smooth background is then obtained by interpolation. An crucial parameter is the size of the sub-frames, because the sub-image must contain, on the one hand, a sufficiently large area for an accurate estimation of the background, but, on the other hand, be small enough in order to provide the required spatial resolution in case of a variable background. We chose the default value provided by the *StarFinder* routine for our images, 22 pixels or $2.94''$. Varying this parameter by $\pm 1''$ had no significant influence on the results.

Images of the background light density and of the extinction (see 3.1.1) corrected background light density extracted in this way are shown in Fig. 5. The horizontal bar that can be seen near the middle of both images is an artefact of the image reduction process and is due to a detector feature that could not be removed (it is also slightly visible in Fig. 1). The uncorrected background light density of the cluster shows a clear extension along the direction southwest-northeast, in agreement with the trend of the extinction. The extinction corrected light density shows a more symmetrical shape of the unresolved background. The brightest star in the field, IRS 7, and the extended source IRS 8 could not be entirely removed from the background and are still visible in the images of the background flux. They were masked in the subsequent analysis. The maximum of the background light before extinction correction (after masking of the residual from IRS 7) is located $\sim 0.15''$ west and $\sim 0.6''$ south of Sgr A*. In the map of the extinction corrected background light, the maximum is not located near Sgr A*, but offset $\sim 5''$ to the southwest. This is due to the high correction factor

introduced by a region of apparently high extinction in this region (an almost north-south running feature, visible in the left panel of Fig. 3). Since this feature is not reproduced in the extinction map derived from NACO intermediate-band imaging (see Fig. 8), we consider it an artefact and mask this region in the analysis of the azimuthally averaged background light density. A possible explanation for this artefact is the presence of diffuse emission due to warm dust in the IRS3E-IRS 2 region (see Fig. 18 and 7 and also Moulitaka et al. 2005) that leads to very red colours of the stars there. After masking of this feature, the maximum light density after applying the extinction correction remains centred on Sgr A*.

The azimuthally averaged background light density in rings of one pixel width is shown in Fig. 6. The left panel shows the uncorrected light density and the right panel the light density corrected for extinction (scaled to the same values as the uncorrected light density). The uncertainty of the average counts results from the uncertainty of the mean of each ring. The main source of uncertainty is the projected distance from Sgr A* because the maps of the background light density have only a limited spatial resolution. The horizontal error bars in the figure correspond to the 1σ -width of a Gaussian function with FWHM equal to the half-width of the sub-frames that were used to derive the background light density. In case of the extinction corrected background light density, the uncertainty due to the low spatial resolution of the extinction map was added quadratically to the horizontal error bars.

Single and broken power-laws were fit to the data, taking into account the uncertainties in both axes. The best-fit results are shown in Fig. 6. Overall, a broken power law provides better fits to the data. The data at distances $\leq 7''$ from Sgr A* prove that a single power law is not a good choice. The formal 1σ uncertainties of the parameters for the power-law index of the cusp, Γ_{cusp} , of the overall cluster Γ_{cluster} , beyond the break radius, and the break radius R_{break} are $\Gamma_{\text{cusp}} = 0.40 \pm 0.05$, $\Gamma_{\text{cluster}} = 0.8 \pm 0.02$, and $R_{\text{break}} = 7.5'' \pm 1.0''$ for the uncorrected light density. After correction for extinction, the best-fit values are $\Gamma_{\text{cusp}} = 0.2 \pm 0.05$, $\Gamma_{\text{cluster}} = 0.95 \pm 0.03$, and $R_{\text{break}} = 6.5'' \pm 0.5''$.

We tested two main sources of systematic uncertainties, that is, a) possible bias introduced by an incorrect subtraction of the sky background during data reduction and b) the accuracy with which *StarFinder* can extract the background flux from the crowded stellar field. Tests were performed with different values for the subtracted sky background. These tests showed that the uncertainty of the sky background is negligible for the slope of the cusp and the value of the break radius. It contributes, however, a 1σ uncertainty of ≤ 0.1 to the slope of the stellar cluster beyond the break radius. In order to test the second source of systematic uncertainty, we produced images with a given, artificial broken power law background structure and added them to the images of the stellar sources and of the residual provided by *StarFinder*. The background was re-extracted from these artificial images and the parameters of broken power-law fits to the azimuthally averaged light density were determined. The 1σ uncertainties estimated from 30 runs (a larger number is problematic due to the high demand of computational time) are $\Delta a_{\text{cusp}} = 0.1$, $\Delta a_{\text{cluster}} = 0.1$ and $\Delta R_{\text{break}} = 1.0''$.

The background light density provides a strong argument why the power-law index of the stellar cluster *must* decrease toward Sgr A*. From the single power law fits of the light density, we can estimate that the surface brightness of the diffuse light near Sgr A* – i.e. after subtraction of the stellar sources – would be $\text{mag}_K \approx 13.5$ per pixel at $R = 0.1''$ and as high as $\text{mag}_K \approx 11.5$ per pixel at $R = 0.01''$. This is clearly not observed because these values are significantly higher than the brightness of the actually observable stars within $\sim 0.5''$ of Sgr A*, the so-called ‘S-stars’, which have K-band magnitudes ≥ 14 .

3.2. AO observations

3.2.1. Source extraction

The great advantage of imaging observations with adaptive optics is, of course, the high spatial resolution, needed to disentangle the crowded point sources in the GC stellar cluster within a few seconds of arc of Sgr A*. However, there are also drawbacks of AO observations, primarily caused by the PSF halos due to incomplete correction and the limited size of the isoplanatic patch ($\sim 15''$). This leads to a PSF that varies across the field. The general consequence is a reduced photometric accuracy. Deconvolution may give rise to numerous spurious sources around brighter stars in the extended wings of their PSFs and in the diffraction spikes due to the spider holding the secondary mirror of the telescope.

The approach chosen in this work was to divide the AO mosaic image into numerous overlapping sub-frames of size $10.8'' \times 10.8''$. Source detection and photometry was conducted with *StarFinder* on these subframes. Since the size of the sub-frames is smaller than the isoplanatic angle, this corresponds to PSF fitting with a spatially variable PSF. The uncertainty of the photometry can be estimated from the measured fluxes of stars that are present in several of the overlapping fields. It was found that the relative photometric uncertainty was $< 10\%$ for more than 86% of the stars.

Figure 7 shows the mosaic of the observations with the intermediate band filter at $2.27\mu\text{m}$ in the upper left panel. In the upper right panel, it shows the background light density determined with *StarFinder*. Clearly, residuals related to bright stars are present in the background. The lower left and lower right panels show the residuals after PSF fitting and background determination. The lower left panel shows the residual image when applying a spatially variable PSF, the lower right panel shows the residual image when a single PSF – determined from bright stars distributed across the entire FOV – is used for the entire image. When only a single PSF is used, there is a clear systematic effect visible in the residuals: Near the guiding star, IRS 7, the residuals are negative, while they become positive at larger distances.

For our analysis of the stellar number counts, we averaged the NACO AO images from the observations at $2.27\mu\text{m}$ and $2.30\mu\text{m}$.

3.2.2. Extinction

NACO intermediate band images at $\lambda = 2.00, 2.06, 2.24$ and $2.27\mu\text{m}$ were used to derive the interstellar extinction. Late- and early-type stars do not have any absorption or emission features at these wavelengths that would significantly affect the photometry in the

IB filters with their relatively broad $\Delta\lambda$. Minor pollution by the CO band head in the $2.27\,\mu\text{m}$ filter, by the *Bry*-line in the $2.24\,\mu\text{m}$ filter, and by the HeI-line at $2.058\,\mu\text{m}$ is possible, but would only account for errors of a few percent.

Since there were not sufficient calibration data available for an accurate *absolute* calibration of stellar fluxes in the intermediate-band filter images, we applied the following method for relative calibration of the fluxes in the different bands. Fluxes at each filter were calibrated using the stars S1, S2, S8, IRS 33N, and W10 which are known as early type stars from spectroscopic measurements by Eisenhauer et al. (2005) or Ott (2004). Rayleigh-Jeans-like spectra could be assumed for the calibration sources. We assumed an extinction value toward the calibration sources of $A_K = 2.8$ mag at $2.157\,\mu\text{m}$ (the value given for S2 in Eisenhauer et al. 2005) and an extinction law $A_\lambda \propto \lambda^{-1.75}$ (see sec. 3.1.1).

The detected stars can be approximated with a blackbody in the observed wavelength range. Interstellar extinction influences the observed spectral energy distribution (SED) of each star via reddening. The colours of the stars between $2.00\,\mu\text{m}$ and $2.27\,\mu\text{m}$ were determined by fitting a line to the measured magnitudes at 2.00 , 2.06 , 2.24 , and $2.27\,\mu\text{m}$. From the assumed extinction law it was then straightforward to calculate the interstellar extinction at $\lambda = 2.157\,\mu\text{m}$ toward the individual sources. Stars with a blue SED were excluded from the measurements because they were considered foreground stars.

In this procedure, the intrinsic colours of the stars have to be known. In this work, only stars with apparent magnitudes $\text{mag}_K \leq 17.75$ were considered. At the GC, main sequence stars of this brightness range can only be O- or B-type stars. About a dozen B-type main sequence stars have been identified near Sgr A* (Eisenhauer et al. 2005). Additionally, there are about 40 spectroscopically identified OB supergiants in the central half-parsec, and a total of maybe 80 massive, young stars (outside of the central arcsecond Paumard et al. 2006). The vast majority of the stars in the FOV covered by our observations, however, are cooler giants or supergiants. We therefore assumed a blackbody temperature of 5000 K for all stars, except for the known early-type stars (taken from Paumard et al. 2006), for which we assumed $T = 20000$ K. An error of 1000 K in the temperature of a cool star or of 10000 K in the temperature of a hot star will lead to an error of just 0.1 mag in the derived extinction at $2.157\,\mu\text{m}$.

In order to keep the uncertainty of the derived extinction low, the median extinction was calculated in circles with $2''$ radius around each pixel in the map. Thus a single extinction value was based on 50-120 measurements, except in the regions with the highest extinction where just slightly more than 20 stars could be detected in such a circle.

The map of the interstellar extinction toward the GC determined in this way is presented in Fig. 8. Circular shapes near the edges of the field are artefacts due to edge effects. The reference wavelength for the extinction map is $2.157\,\mu\text{m}$. The statistical uncertainty at each point in the map is < 0.1 mag, except in the regions of highest extinction, where the uncertainty is < 0.2 mag. The extinction measured at the position of Sgr A*, which is marked by a cross in the figure, is $A_{2.157\,\mu\text{m}} = 2.6$. Compared with the value of 2.8 mag at the position of S2 (Eisenhauer et al. 2005) this indicates a possible systematic error of 0.2 mag.

When comparing our results with the results of Scoville et al. (2003), we find generally good agreement. While with our method, we cannot constrain exactly the absolute value of the extinction without assuming an extinction law, its advantage is that it is not dependent on the presence of line emission in the ISM and provides thus a fairly homogeneous density of measurements across the field. Also, we are not hindered by the brightness of Sgr A* at radio wavelengths. The agreement with the extinction map derived from the seeing limited ISAAC images (Fig.3) is also favourable. The intermediate-band method with the NACO images is certainly the more exact method. Therefore, in the analysis of the ISAAC images, we chose to mask the elongated feature about $8''$ southwest of Sgr A* that was apparent in the ISAAC extinction map (see section 3.1.3). It is not seen on the NACO map.

3.2.3. Completeness correction

With NACO at the 8 m-class VLT, imaging of isolated point sources as faint as $K \sim 19$ is easily achievable with integration times of the order of several tens of seconds. However, when observing the central parsec of the Milky Way, one is confronted with an extremely dense stellar cluster and a large dynamic range due to numerous bright sources distributed across the field: The brightest star, IRS 7, has a K-magnitude of ~ 6.5 and is heavily saturated on all AO images. In addition, there are several dozen sources with a K-magnitude around 10. Also, the field becomes considerably more crowded near Sgr A*. The detection efficiency for faint sources is therefore highly variable (0-100%) across an image. These effects have to be taken into account by determining correction factors that have to be applied to star counts in a given region for a given magnitude.

For determining the incompleteness of the images due to crowding and due to the presence of bright stars we used the technique of adding and recovering artificial stars (see also Genzel et al. 2003b). A properly scaled PSF was added to the original image on grid points spaced $0.5''$ apart. Subsequently, point source extraction was performed with *StarFinder* and the fluxes and positions of the recovered stars were compared with the artificial input stars to see whether a source could be recovered. By shifting the grid and repeating the procedure various times, each image was effectively probed with artificial stars on a $0.1'' \times 0.1''$ -grid (The fine sampling cannot be applied in one step because this would artificially increase crowding). Maps containing the recovered artificial stars (as delta functions, i.e. as pixels of value 1) were divided by maps containing the input artificial stars (as delta functions) to determine the percentage of completeness in the various regions of the images (both maps of delta functions were convolved beforehand with circles of $\sim 0.1''$ radius in order to convert the discrete sampling into continuous maps). We created final maps of the completeness for each magnitude by replacing the completeness at each given pixel in the maps by the average completeness in a $0.25 \times 0.25''$ box centred on that pixel. The uncertainty of the completeness at a given pixel was then taken as the standard deviation in this box. The completeness map for $\text{mag}_K = 16$ is shown in Fig. 9. Table 4 lists the completeness levels inside and outside of a projected radius $R = 8''$ from Sgr A*.

The completeness correction was applied by dividing the delta maps created from the star counts by the square root of the completeness map (a number between 0 and 1) for the corresponding magnitude. The square root was used in order to take into account the Poisson error of the measurements and therefore the increased uncertainty of the correction in areas of low completeness. Areas where the completeness was below 30% were excluded from the analysis, i.e. masked in the maps. Various values were tested for the completeness level where masking was applied. The values 20, 30, and 40% gave similar results, i.e. there is no strong

sensitivity to the exact percentage where masking is applied. Masking was also applied in a circular area of $\sim 2''$ radius centred on the heavily saturated star IRS 7.

3.2.4. Luminosity function

The completeness corrected K-band luminosity function (KLF) is shown in the left panel of Fig. 10. The dashed line is the raw LF and the straight line the completeness corrected LF. The bump at $\text{mag}_K \approx 15.25$ is due to red clump (RC)/horizontal branch (HB) stars. The dotted line indicates the power law index of the LF without the HB bump. It is $\alpha = 0.23$ with a formal fit uncertainty of 0.02. The right panel of Fig. 10 illustrates in a simplified way how much stars of a certain magnitude contribute to the integrated light of the cluster, ignoring the HB bump and assuming validity of the $\alpha = 0.23$ power law index down to $\text{mag}_K = 24$, which would correspond to main sequence stars of about $0.1 M_\odot$ at the GC. This rough illustration shows that while stars with $\text{mag}_K > 16$ may make up more than 98% of the stars in the cluster, they contribute less than 1% to the integrated light.

To first order, the effect of interstellar extinction is that the KLF is shifted along the horizontal axis, depending on the value of A_K . The power law index of $\alpha = 0.23$ determined from the KLF was used in the subsequent analysis when correcting star counts for extinction (see also sections 3.1.2 and 3.1.3).

The location of the KLF peak related to the RC is the reason why, in this work, we chose to bin the stars into magnitude ranges 13.75 – 14.75, 14.75 – 15.75, etc. Thus, the RC stars are largely contained in a single bin.

3.2.5. Two-dimensional stellar surface density

For each magnitude range, maps were created that contained pixel values of 1, i.e. delta functions, at the position of a detected star. Matching masks were created for each magnitude range for areas of extremely low completeness. In these masks, the value of a pixel was set to zero when the completeness at the corresponding position was below 30%. A list of all detected sources was created. If a star was detected at a given distance, it was added to the list with its position, magnitude, the completeness and extinction corrections at the corresponding position, and a correction factor that takes into account the masked area at the corresponding distance from Sgr A* for the corresponding magnitude of the star.

In order to obtain a two-dimensional map of the surface density, an adaptively smoothed map was created. The density at each position in the map was obtained by dividing a constant number by the area of the circle that contained this number of stars (after applying the extinction and completeness corrections). The resulting map is shown in Fig. 11. The number of stars that contribute to the density measurement at each pixel was set to 40, providing a reasonable compromise between high spatial resolution and suppressing small-scale density fluctuations. The necessary smoothing radius varies between about $0.6''$ near Sgr A* to about $1.5''$ at a projected distance of $18''$ from Sgr A*. Correction for masking is difficult to achieve in a two-dimensional surface density map and was therefore not implemented when creating the 2D-figures. Therefore, some areas in Fig. 11 show an artificially low surface density. They are marked with the names of the associated bright stars (e.g., IRS 7, IRS 16NE, IRS 9). Masking of IRS 16NW is probably responsible for the asymmetry of the central cusp that appears slightly offset to the south of Sgr A*. Also, due to masking the density shown in the map for the IRS 13E complex is certainly only a lower limit.

The shape of the cluster appears close to circularly symmetric, but not homogeneous. In Fig. 11, two circles are drawn around Sgr A* that mark projected distances of $3''$ and $7''$. The $3''$ and $7''$ rings appear to contain some 'clumps', i.e. inhomogeneities of increased density. One of these clumps is the IRS 13E cluster, located at a projected distance of $\sim 3.5''$ from Sgr A*. This dense association of bright stars sharing a proper motion in IRS 13E has received much attention (Maillard et al. 2004; Schödel et al. 2005; Paumard et al. 2006).

3.2.6. Radial profile of the number density

Theoretical expectations and our observational data (see Fig. 5 and 11) indicate that the assumption of a spherically symmetric cluster is a good approximation for the central parsecs. This is also supported by the distribution of X-ray point sources (see Muno et al. 2006; Warwick et al. 2006) and large-scale near-infrared observations. Plots of the azimuthally averaged surface density were created by measuring the crowding and extinction corrected counts in rings around Sgr A*. The density was determined in overlapping rings, with their mean distance increasing in steps of one pixel. The width of the rings was chosen adaptively to include 25 stars per smoothing circle, which translates to a variation of the ring width from $\sim 0.5''$ near Sgr A* to $\sim 1''$ at the edge of the field. The value of the mean surface density was determined for each ring. The corresponding uncertainty was calculated from the uncertainties of the completeness correction, the masked area, and of the extinction correction. Because of the width of the rings, the uncertainties of the average densities are fairly small. The uncertainty in the projected distance that is related to each density measurement was determined from the standard deviation of the projected distances of all stars from Sgr A* in the corresponding ring.

The plot of the surface density vs. distance from Sgr A* for stars in the magnitude range $9.75 < \text{mag}_K < 17.75$ is shown in Fig. 12. The straight lines illustrate fits with a single and a broken power law. The dotted line indicates the power-law fit to the ISAAC data alone (see Fig. 4). It can be seen that the broken power law provides a better fit than the single power law. In a certain way this is to be expected because the quality of a fit always improves with the number of parameters. However, it can be seen that the single power law deviates unacceptably from the data inside of about $2''$. This becomes especially drastic if one considers the slope of the cluster far from the cusp, as given, e.g., by the ISAAC data (dotted line in the figure). Since it can be expected that the turnover into the shallow cusp profile is gradual, it is not surprising that a shallower slope of the large-scale cluster is measured when just using the NACO data. The best fit values for the broken power law are a break radius of $6.75 \pm 0.5''$, a power law index

of $\Gamma_{\text{cusp}} = 0.30 \pm 0.05$ for the inner and $\Gamma_{\text{cluster}} = 0.55 \pm 0.05$ for the outer part of the stellar cluster. The broken power law describes the shape of the cluster remarkably well. Possible deviations from the assumed broken power-law in form of apparent under- or over-densities may be present at distances of about $3''$, $5''$, and $7''$.

3.2.7. Star counts vs. light density

Two recent publications on the structure of the central region of the GC stellar cluster apply different methods that lead to different results. On the one hand, Genzel et al. (2003b) used surface number density counts from AO observations with NACO at the ESO VLT and found a power law cusp inside of $10''$ with an increasing stellar density toward Sgr A*. Scoville et al. (2003), on the other hand, used Hubble space telescope data and analysed the diffuse light density of the images by evaluating the median flux in circles around Sgr A*, only taking into account the pixels in the lower 80% of the flux distribution. They found a peak of the flux density at $1'' - 2''$ and a drop inside of $1''$. As is shown in Fig. 10 and noted in section 3.2.4, the total light from the GC stellar cluster is dominated by the contribution from the bright stars. The faintest stars that can be discerned in Fig. 10 of Scoville et al. (2003) are brighter than $\text{mag}_K \approx 15$. Assuming a simple power law LF as in the left panel of Fig. 10, we find that the light from stars fainter than $\text{mag}_K = 15$ contributes $\lesssim 1.5\%$ of the light, while stars brighter than $\text{mag}_K = 13$ contribute $\sim 91\%$ of the total light. Due to the low spatial resolution of the HST in the NIR this suggests that the diffuse light density in the HST images is dominated by the brightest stars and the wings of the PSF from the brightest stars, even if the brightest 20 – 50% of the pixels are discarded.

This hypothesis was tested in a simple way by creating artificial images using the lists of identified stars in the high-resolution NACO/VLT AO images combined with the appropriate point spread function and the known magnitudes of the stars. Two maps were created, one containing stars in the magnitude range $9.75 - 17.75$, the other one in the range $14.75 - 17.75$. The surface density of the light was determined in the same rings that were used to extract the number density (see section 3.2.6 for details). Completeness and extinction corrections were taken into account. Following Scoville et al. (2003), the light density was determined by taking the median of the pixel brightness distribution in the rings and by taking into account only the fainter 80% of the pixels.

The results of this test are shown in Fig. 13. In the left panel, the radial light density extracted from the map with stars $9.75 \leq \text{mag}_K \leq 17.75$ is compared to the corresponding number density (the average light density was scaled to the average number density). In the right panel a similar plot is shown for stars $14.75 \leq \text{mag}_K \leq 17.75$. The plot that includes the bright stars looks fairly similar to Fig. 12 shown in Scoville et al. (2003). The density maximum is reached at projected distances of $1'' - 3''$ from Sgr A*. The peak of the light density and its decrease inside of $1''$ are less pronounced in Fig. 13 than in the corresponding plot by Scoville et al. (2003). The probable cause is that in this work, we only considered stars fainter than $\text{mag}_K = 9.75$. The star IRS 16NE, with $\text{mag}_K \approx 9.0$ is located at a projected distance of just $3.0''$ from Sgr A*. It was not considered in our test, but is present in the HST image. It is evident that the bright stars have a significant influence on the surface light density. The surface light density can therefore be misleading when determining the shape of the GC stellar cluster. The excess light density at projected distances $1'' - 5''$ from Sgr A* is probably related to the presence of bright, young stars in this region (e.g., Paumard et al. 2006). In marked contrast, the trend of the azimuthally averaged light density of the faint stars is very similar to the surface number density, as expected for a homogeneous stellar population.

The analysis of the seeing limited ISAAC data (see section 3.1.3) shows that the diffuse light density can be examined well by extracting the point sources via PSF fitting combined with simultaneous background estimation. A particular difficulty with AO imaging data is, however, the spatially variable PSF. Combined with the extreme source density in the central arcseconds, this has the effect that estimating the wings of the PSF is subject to possibly significant uncertainties. This can lead to considerable residuals present in the smooth, fitted background light density in the vicinity of brighter stars (see Fig. 7, upper right panel). By rejecting the brightest 50-80% of the pixels, similar to the analysis in Scoville et al. (2003), however, the influence of these residuals of the bright stars can be minimised when extracting the azimuthally averaged light density. We applied this method and show the resulting plots of the background light density vs. distance from Sgr A* in Fig. 14. Both the raw and extinction corrected background light density can be fitted well with a broken power law. The parameters for the extinction corrected data are $R_{\text{break}} = 4.0 \pm 0.8''$, $\Gamma_{\text{cusp}} = 0.15 \pm 0.07$, and $\Gamma_{\text{cluster}} = 0.85 \pm 0.07$. Here, the uncertainties include the formal uncertainty as well as the uncertainty due to the reliability of the extraction of the background light from the AO images. The latter was tested by creating artificial images with a given background, and varying the break radius and the power-law indices (as described for the seeing-limited data in section 3.1.3). The background could be reliably recovered.

3.3. Adaptive-kernel estimates of the surface and space densities

Estimating the surface density by counting stars in bins has a number of disadvantages (e.g. Scott 1992): the estimates are discontinuous, the bias-variance tradeoff is far from ideal, confidence intervals on the density are difficult to compute, etc. Also, it is impossible in principle to differentiate a binned density profile, which means that quantities like the space density are impossible to compute unless parametric forms are fit.

All of these shortcomings can be addressed by adopting techniques from nonparametric function estimation theory. Here, we apply an adaptive kernel method to estimate Σ and ρ (Merritt & Tremblay 1994). We imagine that each star on the 2D image is replaced by a circularly-symmetric Gaussian kernel. Averaging this kernel over angle at fixed distance from the black hole generates a 1D, asymmetric kernel which can be used to compute an estimate of $\Sigma(R)$:

$$\Sigma(R) = \sum_{i=1}^N \frac{w_i}{h^2} K(R, R_i, h), \quad (2)$$

$$K(R, R_i, h) \equiv \frac{1}{2\pi} e^{-(R_i^2 + R^2)/2h^2} I_0(RR_i/h^2). \quad (3)$$

Here, R_i is the projected radius of the i th star, w_i is the weight associated with the i th star, and h is the kernel width, roughly analogous to the bin width; I_0 is the modified Bessel function. We varied the kernel width as $R^{0.8}$, or roughly as $\Sigma^{0.5}$; the mean value of h was chosen so as to give roughly the same degree of smoothing as in the binned estimates of Figs. 5 and 6. Estimates of the space density $\rho(r)$ were obtained by applying Abel's formula directly to the Σ estimates, using a larger value of h in order to compensate for the increased variance due to the differentiation. Bootstrap confidence intervals on all quantities were generated via resampling (Efron 1982).

Figure 15 shows the results, compared with the $\Sigma \sim R^{-3/4}$ and $\rho \sim r^{-7/4}$ Bahcall-Wolf predictions. The mean indices are lower than predicted, and exhibit what appear to be statistically significant wiggles. The general structure of the cluster, i.e. a broken power-law with a break radius around $7''$ and a rather flat cusp can be seen in the kernel estimates as well.

4. Discussion

4.1. Contamination by the discs of young stars

Considering the one/two discs of young stars discovered and described by Levin & Beloborodov (2003) and Genzel et al. (2003b) and described in detail by Paumard et al. (2006), the question arises about the extent by which the stellar surface density derived in this work is contaminated by stars in these discs. It is not straightforward to assess how many young stars contribute to the surface density at each radius. However, we can give a rough estimate by using the information in Paumard et al. (2006). In their Fig. 13, they plot the luminosity functions of the spectroscopically identified young stars. They find a very flat slope, from which they conclude that the IMF of the stellar discs must be much flatter than the slope of the Miller-Scalo IMF. Extrapolating from their KLF between K-magnitudes 11 and 14 shows that the surface density of faint ($K = 16 - 17$) stars that may belong to the young stellar discs should be only a factor 5-10 higher than the surface density of the brighter stars. This would result in a surface density of faint young stars of $\leq 2 \text{ arcsec}^{-2}$ within $2 - 5''$ of Sgr A*.

Alternatively, Paumard et al. (2006) also show that the surface density profile of the discs is very steep, with an exponent of about -2 (see their Fig. 6). They have spectroscopically identified the brighter stars with $\text{mag}_K < 15$. Taking the density of the discs between projected radii of $2'' - 5''$ and scaling it by factors ~ 10 -20 in order to adjust it for the fainter stars (using the KLF of Paumard et al. 2006), surface densities of 1-2 young stars arcsec^{-2} within $2 - 5''$ of Sgr A* are obtained. Therefore, since the faint stars at magnitudes 15-17 dominate the star counts, the surface density plots in Fig. 12 should not be contaminated significantly by the stars in the young stellar discs. An exception are the stars with K-magnitudes between 14 and 15. As Eisenhauer et al. (2005) have shown, stars in this brightness range within about $0.5''$ of Sgr A* appear to be B-type main sequence stars.

The concentration of bright, young, massive stars in the stellar discs within a few arc seconds of Sgr A* is, however, reflected nicely in the plot of the surface light density shown in Fig. 13. The light density shows a clear excess at projected distances between about $1''$ and $4''$ from Sgr A*.

4.2. Mean stellar mass probed, mass segregation

Figure 16 shows the predicted K-band luminosity function (KLF), the mean stellar age and the mean stellar mass for all stars and the old ($> 1 \text{ Gyr}$) stars, as function of their K-band luminosity. This population synthesis model for the central parsec (Alexander & Sternberg 1999; Alexander 2005) assumes a continuous star-formation history over the lifetime of the Galaxy with a "normal" initial mass function (here Miller & Scalo 1979). The model is based on the $Z = 1.5Z_\odot$ stellar evolution tracks of Schaller et al. (1992) and Girardi et al. (2000). The continuous star formation history is indicated by the very good match between this model and the observed KLF (evolved red giants and massive blue giants) in the inner GC (Alexander & Sternberg 1999), as well as by models of the luminosity in the GC on the $\sim 50 \text{ pc}$ scale (Figer et al. 2004). The model does not take into account the recent star formation processes reflected in the two discs of young, massive stars in the inner $10''$ (e.g. Genzel et al. 2003b). However, this should only affect significantly the bins brighter than $\text{mag}_K \leq 13$ (see also discussion in section 4.1).

The mean mass is quite constant in the range ~ 13 -17 mag, $\langle M_\star \rangle \sim 3 M_\odot$ (main sequence life span $\sim 0.5 \text{ Gyr}$), with a distinct drop to $\langle M_\star \rangle \gtrsim 2 M_\odot$ at $K \sim 15.5 \text{ mag}$, due to the concentration of red clump horizontal branch giants (main sequence life span $> 1 \text{ Gyr}$) in that magnitude range, as observed in the measured KLF (see Fig. 10 in this work and also Fig. 9 in Genzel et al. 2003b). The mean mass of the entire population (including fainter stars and remnants) is $\langle M_\star \rangle = 0.5 M_\odot$ (Alexander 2005, table 2.1). Thus, the mean star included in our counts is expected to have an intermediate mass between the typical numerous low mass objects, and the rarer massive stars and stellar mass black holes, which probably dominate the very centre due to mass segregation (Morris 1993; Miralda-Escudé & Gould 2000; Hopman & Alexander 2006; Freitag et al. 2006). In the restricted K -range near the horizontal branch feature, $15 \leq K \leq 16 \text{ mag}$, up to 80% of the stars are old, and are thus more likely to have attained their steady-state distribution. The mean mass of the old stars is $\langle M_\star \rangle \simeq 1.5 M_\odot$. Mass segregation substantially shortens the relaxation time below the typical value estimated in section 4.5 because it increases the mean stellar mass (see e.g. section 3.2.1 in Alexander 2005). A numerical model of mass segregation in the GC (Hopman & Alexander 2006) indicates that the relaxation time falls from $\sim 1 \text{ Gyr}$ at 0.4 pc to $\sim 0.4 \text{ Gyr}$ (the typical lifespan of a $3 M_\odot$ star) at 0.02 pc . The HB/RC progenitors ($< 2 M_\odot$) have lifespans $> 1 \text{ Gyr}$ and are thus expected to be well-relaxed and segregated. The dynamical state of the $\sim 3 M_\odot$ stars brighter and fainter than the RC giants is less certain, since their lifespans are of the same order of magnitude as the relaxation time, but they could plausibly be segregated to a substantial degree. We thus expect stars in the 15-16 magnitude range to have the shallowest slope in comparison with stars immediately brighter and fainter.

Based on these theoretical predictions, we examined the azimuthally averaged surface density for magnitude bins of 13.75 – 14.75, 14.75 – 15.75 (HB/RC stars), and 16.75 – 17.75. In the KLF shown in the left panel of Fig. 10 one can see that the intermediate bin includes most HB/RC stars, while the bin with the faintest stars should be largely free of HB/RC stars. The bin for the brighter stars may contain some HB/RC stars, but was chosen because it contains a statistically more significant number of stars than the next brighter bin. The resulting number density plots for the different stellar types, along with broken power law fits, are shown in Fig. 17. We find systematically different slopes on the $\geq 3\sigma$ level. Stars brighter or fainter than the HB/RC stars have somewhat shallower power-law indices outside of $\sim 10''$. Possibly, this is due to star formation activity. As qualitatively anticipated by the stellar mass model (Fig. 16) and as predicted for a relaxed multi-mass cusp (Bahcall & Wolf 1977), we find a shallower cusp for the low-mass stars that dominate the bin $\text{mag}_K = 15 - 16$. However, the slope of the cusp shallower than predicted by the Bahcall-Wolf solution, and the difference between this slope and that of the adjacent fainter and brighter magnitude bins, which are dominated by more massive is much larger than found in the numeric simulations of Freitag et al. (2006) for $2M_\odot$ and $3M_\odot$. These deviations from the theoretical predictions cast some doubt whether the observed trend in the cusp slopes is due to mass segregation, or perhaps reflects different dynamical histories for the old, low-mass stars and young and massive ones.

There appears a curious feature in the surface density of the intermediate-bright stars, a “trough” or under-density, at a projected radius of about $5''$. It may be related to a lack of HB/RC stars at this distance. The data and power-law fit presented in the middle panel of Fig. 17 indicate that the feature is clearly significant on the $> 5\sigma$ level (very small error bars would result when averaging the density between, e.g., $4'' - 6''$). The dip around $5''$ is also present in the surface density plots presented by Eckart et al. (1993, , their Fig. 4) (although with a low significance) and Genzel et al. (2003b, , their Fig. 7). We do not detect this feature in the surface density of the unresolved background, which is expected to trace the stellar population with K-magnitudes $> 17 - 18$, and thus stellar masses comparable to or lower than the HB/RC stars. We conclude that the feature is therefore due to an under-density of HB/RC stars at this distance or – alternatively – an over-density of similarly bright stars of a different, possibly early type at slightly larger and smaller distances. Early type stars could be related to the few million year-old starburst in the central parsec (e.g., Allen et al. 1990; Krabbe et al. 1995; Paumard et al. 2006). Genzel et al. (2003b) find a clockwise and a counter-clockwise rotating ring of young stars in the central half-parsec with characteristic radii of $2'' - 4''$ for the clockwise and $4'' - 7''$ for the counter-clockwise one, respectively. If the systems of young stars are ring-like with most stars concentrated at these radii then there could exist an over-density of intermediate-bright stars at the corresponding distances. In fact, as discussed in the section above, the star counts in the brightness range of the HB/RC stars may be contaminated in a non-negligible way by young stars in the innermost arcseconds. More detailed spectroscopic information is needed in order to examine this feature of the cluster further.

4.3. Clumpiness of the cluster

The analysis of the surface density map of the GC stellar cluster showed that besides the previously known density concentration of stars in the IRS 13E cluster there appear to exist several other significant localised concentrations or clumps of stars. Recent observations and theoretical work indicate that the formation of the young stars in the GC has probably occurred in massive accretion discs (see Nayakshin et al. 2006; Nayakshin 2006; Paumard et al. 2006). The identification of dense groups of co-moving stars in the GC cluster can then be interpreted in the sense that fragmentation of the discs and subsequent star formation in these fragments may produce fairly large sub-groups of stars. Highly clustered star formation in the discs of young stars is indeed indicated in simulations (S. Nayakshin, private communication). Detailed spectroscopic information and proper motion studies are needed in order to clarify the nature of the clumps in the cluster.

4.4. Extinction and structures in the ISM

Figure 18 shows contours of the interstellar extinction (see Fig. 8) superposed on a NACO L'-band ($3.8\mu\text{m}$) image. The so-called mini-cavity to the southwest of Sgr A* can be distinguished clearly in this image and is indicated by a white dashed line. Linear filaments, possibly shock fronts, mark its western edge. It has been suggested that the mini-cavity might be created by fast winds from the HeI-stars in the the central star cluster or - more speculative- by an outflow from Sgr A* (Lutz et al. 1993; Melia et al. 1996; Yusef-Zadeh et al. 1998).

It is interesting to note that there is a narrow, channel-like feature aligned southwest-northeast running right across Sgr A* and toward the mini-spiral. Cometary-like sources (indicated by blue arrows in the Figure) are aligned with this structure and point right at Sgr A*. Mužić et al. (in prep.) discuss these features along with filamentary structures and their proper motions in L'-band images and relate them to a putative outflow from the central arcseconds.

In theoretical models that are used to understand accretion and emission processes near Sgr A*, so-called RIAF models (radiatively inefficient accretion flow, see, e.g., Quataert 2003) the extremely low accretion efficiency is almost inevitably related to the presence of outflows (see also the ADIOS model by Blandford & Begelman 1999). Also, there a theoretical and observational arguments that favour the presence of a jet in Sgr A* (e.g., Melia & Falcke 2001; Markoff et al. 2001; Yuan et al. 2002; Bower et al. 2004). As for the orientation of the outflow, Eckart et al. (2006b) and Meyer et al. (2006b) note that the electric field vector during a NIR flare was oriented along the direction southwest-northeast, similar to the direction of the channel-like feature that is centred on Sgr A*. A very similar angle was found during a second NIR flare event (Meyer et al. 2006a; Trippe et al. 2006). In combination with the theoretical considerations and the other evidence for an outflow from the region near Sgr A*, the low-extinction channel found by us may represent a new piece of evidence for the existence of an (aligned) outflow.

4.5. Overall structure of the cluster

We have used different methods to derive the structure of the GC star cluster. These methods include analyses of star counts as well as of the diffuse background light on seeing-limited and AO-assisted images. All analyses have shown clearly that a single power-law is insufficient to describe the cluster, while a broken power-law provides a very good approximation. Table 5 summarises the parameters of the cluster as they were determined by the various methods. From these independent measurements average values of the parameters were determined with their estimated 1σ uncertainties. These are listed in the last line of Table 5. They are a break radius $R_{\text{break}} = 6.0'' \pm 1.0''$ (0.22 ± 0.04 pc), a power-law index for the cusp of $\Gamma_{\text{cusp}} = 0.19 \pm 0.05$, and a power-law index for the cluster outside of the break radius of $\Gamma_{\text{cluster}} = 0.75 \pm 0.1$. These values are also in good agreement with the values derived by the kernel method (see Fig. 15).

The determined slope of the large-scale cluster is in good agreement with what has been found already by Becklin & Neugebauer (1968), and later by Catchpole et al. (1990), Eckart et al. (1993), Haller et al. (1996), Genzel et al. (2000), or Launhardt et al. (2002). Also, note that Warwick et al. (2006) find that a part of the diffuse X-ray radiation within $3' - 12'$ around Sgr A* is probably caused by faint point sources with a surface brightness that falls off as $R^{-0.87 \pm 0.06}$. Also, Muno et al. (2006) find that the X-ray point sources follow a close to isothermal power-law index in the central parsecs of the GC.

The slope of the large-scale cluster indicates therefore that it may be close to the structure of a singular isothermal sphere. An isothermal model for the large scale cluster would also be in good agreement with the finding of a constant velocity dispersion of late-type stars at projected distances outside of 0.2 pc (see Figer et al. 2003).

As concerns the slope of the cusp, Genzel et al. (2003b) derived a value of $\Gamma = 0.4 \pm 0.1$ for the power-law index of the projected surface density, while we obtain a somewhat shallower cusp with $\Gamma = 0.19 \pm 0.05$. The shallow shape of the cusp is certainly an important factor in explaining why it could not be found by observations with smaller telescopes and without the aid of adaptive optics. Detection of the cusp is additionally hindered by the need for a high dynamic range due to the presence of the bright, young stars such as in the IRS 16 and IRS 13 complexes in the inner arc seconds. Therefore, previous publications often assumed a flat core (Eckart et al. 1993; Haller et al. 1996; Genzel et al. 1996), with a core radius similar to the break radius determined in this work and in Genzel et al. (2003b).

The kernel method (see Fig. 15) gives a more detailed impression of the structure of the inner part of the cluster, i.e. the cusp. The average slope derived with the kernel method agrees well with the power-law fit described above. The kernel estimator shows that there may be significant variations present in the slope of the cusp, but that overall, a description by a power-law is fairly good.

The different power-law for the cusp and the improved accuracy of its value is due to the improved data set and refined analysis in this work. Just to mention a few improvements: use of a uniform data set, PSF fitting with a spatially variable PSF, extinction correction, masking of regions with extremely low completeness, no binning of the counts, analysis of star counts as well as of the diffuse background light.

It is interesting to note that the cluster profile based on star counts, presented by Eckart et al. (1993), showed a core radius of $3.8''$. Their data were dominated by stars with a brightness $\text{mag}_K = 14 - 15$, very similar to the density profile shown in the middle panel of Fig. 17 that agrees remarkably well with the results of Eckart et al. (1993).

Although a broken power-law fit provides a satisfying description of the structure of the GC cluster, we would like to mention that the stellar density (Fig. 12, 15 and 17) and also the profile of the light density of the faint stars (right panel of Fig. 13) indicate that there may be a separate structure present in the central arcsecond around the black hole. This is indicated by the steeper slope of the number and light density in this region. Eisenhauer et al. (2005) have found that the central arcsecond appears to be dominated by B-type main sequence stars. The crowding of stars of this peculiar type (so far not reported in significant numbers at larger distances) supports the idea that the region within $1''$ of Sgr A* is dominated by a unique cluster structure with a special stellar population. The central arcsecond also stands out clearly in the 2D-density map in Fig. 11. The cusp is possibly dominated by stellar black holes (see, e.g., Morris 1993; Miralda-Escudé & Gould 2000; Mouawad et al. 2005; Amaro-Seoane et al. 2004; Freitag et al. 2006; Hopman & Alexander 2006). The B-stars in the S-cluster around Sgr A* (Eisenhauer et al. 2005), are fairly massive stars and could thus coexist with these stellar remnants. These massive stars must be young and therefore not dynamically relaxed. They may represent a separate entity within the cusp and it is not yet clear how they are related to the overall structure of the GC star cluster.

4.6. Comparison with theory

4.6.1. Shape of the cluster

A super-massive black hole is predicted to dominate the gravitational potential within a region $r \leq r_h$, where r_h is customarily defined as the radius containing a mass in stars equal to twice the black hole mass (see Merritt 2006). As for the extent of the cusp, the Bahcall-Wolf cusp (for a single-mass population) is predicted to extend out to a distance of $0.1 - 0.2 r_h$ from the black hole (see Preto et al. 2004; Merritt & Szell 2006).

The two-body relaxation time for a single stellar mass population, i.e. the time for gravitational encounters to set up a locally Maxwellian velocity distribution, is roughly

$$t_r = \frac{0.34\sigma^3}{G^2 m \rho \ln \Lambda} \quad (4)$$

(Spitzer 1987). Within the cusp, $r \ll r_h$, the gravitational potential is dominated by the black hole; thus $\sigma \propto r^{-1/2}$. Based on Figure 15, the space density in the central 0.5 pc is reasonably well approximated by $\rho \sim r^{-3/2}$, which makes t_r approximately independent of radius in the cusp. Assuming solar-mass stars and setting $\ln \Lambda \approx \ln(r_h \sigma^2 / 2Gm) \approx \ln(M_\bullet / 2m) \approx 14$ (Preto et al. 2004), the relaxation time in the cusp is roughly 5×10^9 yr. It may in fact be lower by a factor of a few because the stars in the

observed brightness range are fairly massive. Hence, the relaxation time is lower than the age of the Milky Way. One therefore expects to find a collisionally relaxed distribution of orbital energies within the cusp, i.e. the Bahcall & Wolf (1976) solution should hold for a single-mass stellar population. Core collapse, which requires a much longer time of $\sim 10^2 t_r$, is not important.

The slope of $\rho(r)$ is shallower than predicted by the (single-mass) Bahcall-Wolf form, $\rho \sim r^{-7/4}$ (Fig. 7). One possible reason, as discussed by Merritt & Szell (2006), is that the cusp may not have existed for a long enough time for a steady-state energy distribution to have been reached. Those authors estimate that a time of nearly 10^{10} yr is required for the stars around the GC black hole to attain a collisional steady state. Depending on the time since the last event that significantly disrupted the cusp – e.g. infall of an intermediate-mass black hole – the cusp may still be evolving toward the Bahcall-Wolf form. Another reason for the cusp slope to be $< 7/4$ is that the stars we are probing in this work have masses in the range $2 - 3 M_\odot$ (see section 4.2). If the centre of the cluster is dominated by stellar black holes, which may have spiralled in there due to mass segregation, then the masses of the used tracer stars are lower than the average point mass in the nuclear cluster, which would lead to a slope flatter than the Bahcall-Wolf solution. Another possible explanation for the faint slope of the cusp may be the importance of collisions because of the high density in this region (see section 4.6.2 below).

We would like to note that we do not observe any flattening of the cusp at the smallest radii as it would be expected because of the onset of stellar collisions in the dense environment of the cusp (see, e.g., Murphy et al. 1991; Alexander 1999; Amaro-Seoane et al. 2004). Murphy et al. (1991) show that for their model 3B, which corresponds most closely to the enclosed mass and mass densities derived in this work, the region where the density distribution is flattened by collisions has a radius $r \leq 10^{-3}$ pc. This corresponds to less than $0.1''$ at the distance of the GC and can therefore not be reasonably resolved by the present observations.

We have found a break radius – which corresponds roughly to the extent of the cusp – of $6.0'' \pm 1.0''$ or 0.22 ± 0.04 pc for the GC stellar cluster (see Table 5). It is important to note that this break radius is also valid for the HB/RC population, that is, for the oldest stars in our sample that should represent best the shape of the dynamically relaxed population. The same break radius is also found (within the corresponding uncertainties) for the diffuse background light, i.e., the faint, lower-mass, unresolved stellar population (see Figures 6 and 14). From this break radius we obtain $r_h \approx 30'' - 60''$ or $r_h \approx 1.1 - 2.2$ pc, if we assume that $R_{\text{break}} \approx 0.1 - 0.2 r_h$.

4.6.2. Enclosed mass

For estimating the enclosed mass at the GC on parsec scales, a commonly used assumption is that the circumnuclear disk (CND) is a rotating ring of gas, subject only to gravitation. The GC circumnuclear disk is commonly assumed to have a radius of about 1.6 pc and is interpreted to rotate with a circular velocity of about 110 km s^{-1} (Guesten et al. 1987; Jackson et al. 1993; Christopher et al. 2005). From these numbers, one can estimate a total enclosed mass of $\sim 4.5 \times 10^6 M_\odot$, of which $\sim 3.6 \times 10^6 M_\odot$ are due to the black hole. With these values r_h should be roughly 4 – 6 pc, or $110 - 160''$, and the predicted extent of the cusp consequently a factor of a few larger than what is actually observed. These numbers are of course subject to the assumption that the rotation of the CND is a suitable tracer of the enclosed mass.

However, there are other ways to estimate the enclosed mass at large distances. Reid et al. (2003) and Reid et al. (astro-ph/0612164) present highly accurate measurements of the velocity of the maser star IRS 9, that is located at 0.33 pc in projection from Sgr A*. Under the assumption that IRS 9 is on a bound orbit, an enclosed mass of at least $4.4 \times 10^6 M_\odot$ is required (scaling the mass estimate of Reid et al. to the 7.6 kpc distance of the GC assumed in this work). This would require a much higher mass than what is derived assuming that the CND is a suitable tracer of the enclosed mass.

An alternative way of estimating the enclosed mass is using the measured line-of-sight velocity dispersion, σ_z , of the old, presumably relaxed stellar population. Figer et al. (2003) present high precision spectroscopic measurements that show that σ_z is constant with a value of $100.9 \pm 7.7 \text{ km s}^{-1}$, down to projected distances of at least 0.2 pc from Sgr A*. Similar to Figer et al. (2004), we have used the Bahcall-Tremaine mass estimator

$$M_{\text{BT}}(R) = \frac{16}{\pi G N} \sum_i^N v_z^2 R_i \quad (5)$$

(Bahcall & Tremaine 1981) to determine the enclosed mass. Here, G is Newton's gravitational constants, N is the number of stars within a projected radius R , R_i is the projected radius of the i -th star, and v_z its spectroscopically measured line-of-sight velocity. Assuming isotropic stellar orbits, a constant velocity dispersion, σ_z , and a stellar surface density given by a broken power-law with the parameters as listed in the last line of Table 5, the enclosed mass at projected distance R is thus:

$$M_{\text{BT}}(R) = \frac{16\sigma_z^2}{\pi G} \frac{\int_0^R (R'^{2-\Gamma}/R_{\text{break}}^{-\Gamma}) dR'}{\int_0^R (R'^{1-\Gamma}/R_{\text{break}}^{-\Gamma}) dR'} \quad (6)$$

The power-law index, Γ , assumes the corresponding values inside and outside of the break radius R_{break} . We assumed a constant velocity dispersion outside and a Keplerian increase inside the break radius. The resulting mass estimate at short distances from Sgr A* ($2.6 \pm 0.3 \times 10^6 M_\odot$) was corrected to the precisely known mass of the central black hole of $3.6 \pm 0.3 \times 10^6 M_\odot$ (Eisenhauer et al. 2005). Note that the correct black hole mass can be obtained if the break radius were located at 0.3 pc. The black line in the upper panel of Fig. 19 shows our estimate of the enclosed mass vs. projected distance. The dashed lines indicate the uncertainty of the measurements (it is dominated by the uncertainty of σ_z). The up-pointing arrow at $R = 0.33$ pc is the enclosed mass estimate from IRS 9 (Reid et al., astro-ph/0612164; their value was adapted to a GC distance of 7.6 kpc, that is used in this work). The error bars at 1.6 pc and 2.0 pc are mass estimates based on the assumption of a circularly rotating CND with a radius of 1.6 pc and a rotation velocity of 110 km s^{-1} and a radius of 2.0 pc and a rotation velocity of 130 km s^{-1} , respectively (see Guesten et al.

1987; Christopher et al. 2005). As mentioned by Rieke & Rieke (1988), the uncertainties of mass estimates based on the CND are probably large due to the presence of significant non-circular motions within the CND. As can be seen, the mass estimate based on the velocity dispersion of the late-type stellar population agrees fairly well with the lower mass estimate based on IRS 9, but disagrees on a $> 5\sigma$ level with the estimates based on the assumption of a circularly rotating CND. Our estimate of the enclosed stellar mass agrees very well with the estimates by Haller et al. (1996, see their Figs. 8 & 9). Haller et al. (1996) determined the enclosed mass distribution for the central 300 pc of the Milky Way. They assumed a pseudo-isothermal structure of the stellar cluster, with a power-law exponent of $\gamma = -1.8$, very similar to this work. Also, they used a core radius of $7''$ for the cluster, in very good agreement with the break radius determined by our analysis.

Similar mass estimates are obtained from stellar proper motions. Ott (2004) present an analysis of stellar proper motions within $9''$ of Sgr A*. They also find an approximately constant velocity dispersion of about 100 km s^{-1} (one dimensional value) outside of a projected radius of about $6''$, with a Keplerian increase inside of this distance. They estimate the enclosed mass vs. projected distance from Sgr A* with the help of various mass estimators and always find fairly high values, in agreement with the lower mass estimate based on IRS 9 and in agreement with the enclosed mass estimate shown in the left panel of Fig. 19. The observation that the velocity dispersion is constant outside of $6''$ or about 0.2 pc indicates that the gravitational field is dominated by the point mass of the black hole only inside of this distance.

All mass estimates that are based on stellar tracers are significantly higher than what one can derive from the assumption of a CND that is in circular rotation. Stars are commonly accepted to be more reliable tracers of the gravitational field than gas because they are point-like particles and are not subject to forces from magnetic fields, winds, or collisions. We therefore believe that the estimates of the enclosed mass in the GC must be corrected significantly upwards, contrary to what has been published earlier (e.g., Schödel et al. 2003) because these earlier estimates were based on measurements of gas velocities and an incomplete knowledge of the velocity dispersion of the stellar cluster (a values of $\sim 50 \text{ km s}^{-1}$ was assumed in previous models).

The green line in Fig. 19 indicates the enclosed mass after subtraction of the black hole mass. The red line is an estimate of the mass of the visible stellar cluster. Here, an average mass of $3 M_{\odot}$ was assumed for the detected stars (see section 4.2). In order to estimate the mass of the diffuse, unresolved component of the cluster, we assumed a mass-to-luminosity ratio of $2 M_{\odot}/L_{\odot}$ at $2 \mu\text{m}$ (Haller et al. 1996). Note that other authors (e.g. Philipp et al. 1999; Kent 1992) find a lower value of $1 M_{\odot}/L_{\odot}$. This would result in a lower estimated mass of the visible stellar cluster. The M/L ratio was combined with the measured surface brightness of the diffuse background light, which was estimated to $0.007 \text{ Jy arcsec}^2$ at the break radius. The systematic uncertainty of the background light density is about 30% as can be estimated by a comparison of Figs. 6 and 14. The main sources of the uncertainty are the choice of the calibration sources and the background subtraction in the ISAAC data. To correct for the nuclear bulge, a surface brightness of $0.0006 \text{ Jy arcsec}^2$ was subtracted (value at $\sim 10 \text{ pc}$ taken from Philipp et al. 1999).

The black line in the right panel of Fig. 19 shows the volume density of the estimated enclosed mass:

$$2.8 \pm 1.3 \times 10^6 M_{\odot} \text{ pc}^{-3} \times \left(\frac{r}{0.22 \text{ pc}} \right)^{-\gamma}, \quad (7)$$

where r is the distance from Sgr A*, $\gamma = 1.2$ the power-law index inside 0.22 pc and $\gamma = 1.75$ the power-law index outside of 0.22 pc . The resulting densities are similar to the values given in Genzel et al. (2003b). The red line shows the estimated density of the visible stellar cluster. The dashed lines indicate the 1σ uncertainties. The data show that the estimated mass density is possibly a factor of roughly 2 higher than the density of the visible stellar cluster. Of course, the uncertainties are large. They can be improved by more precise measurements of the diffuse surface brightness, the velocity dispersion, and of the central black hole mass. The inferred mass densities are in good agreement with the extent of the cusp derived in this work. The left panel of Fig. 19 shows that the cluster contains twice the mass of the black hole within a projected radius of $< 2 \text{ pc}$. This is in good agreement with the $r_h = 1.1 - 2.2$ predicted from the measured extension of the cusp ($0.22 \pm 0.04 \text{ pc}$). Also, the fairly flat power-law of the cusp $\Gamma = 1.2 \pm 0.05$ may be related to a high central density because flat cusps are created when collisions become important (Murphy et al. 1991).

There are certain caveats to keep in mind, i.e. basic assumptions that we used for our mass estimate: (a) The assumption of a constant velocity dispersion outside of 0.22 pc . This assumption seems, however, well justified because our estimation of the enclosed mass agrees well with the data by Haller et al. (1996), who used velocity dispersion measurements out to 300 pc (see, however, Launhardt et al. 2002). Also, the basic conclusion, that there is possibly a significant amount of non-stellar matter present stays valid if we limit the analysis only to distances within 1 pc , based on the velocity dispersion measurements by Figer et al. (2003) and Genzel et al. (2000). (b) Assumption of the given structure of the cluster. As for the visible cluster, a power-law index of 1.8 is, however, well established (see discussion in this work and, e.g., Becklin & Neugebauer 1968; Catchpole et al. 1990; Eckart et al. 1993; Genzel et al. 2003b). Variations of the cluster slope within the uncertainties will not have any significant influence on our estimate. The extent and power-law index of the cusp are only of minor importance, due to its small extent and the small total mass enclosed in this volume. (c) Validity of the BT mass estimator. The use of the BT mass estimator seems justified because it provides the correct mass for the central black hole (within a factor of 30%) and it agrees well with other mass estimators (see, e.g., tests by Ott 2004). (d) Assumption of a given M/L ratio for the stellar cluster. It seems, however, well established and we have used the more conservative one of the values, i.e. the one that results in a larger stellar mass, established by observations (see Philipp et al. 1999; Kent 1992).

What can the enclosed extended dark mass be composed of? Primary candidates are dark matter and stellar remnants. As for dark matter Bergström et al. (2006) inferred upper limits on the density of dark matter using the density profile of cold dark matter of Navarro et al. (1996). The resulting density of $66 M_{\odot} \text{ pc}^{-3}$ at a distance of 1 pc from Sgr A* is by several orders of magnitude too small in order to have a measurable influence.

Due to their high mass, stellar-mass black holes sink toward the GC via dynamical friction. Several authors have estimated the amount of mass in form of stellar-mass BHs in the central parsec (e.g., Morris 1993; Miralda-Escudé & Gould 2000). Miralda-

Escudé & Gould (2000) find that about 25,000 stellar-mass BHs may be present in the central parsec, corresponding to roughly $2.5 \times 10^5 M_\odot$. Similarly low numbers are found by Freitag et al. (2006) and Hopman & Alexander (2006). A much higher value is derived by Morris (1993), who calculate that of the order $10^6 M_\odot$ may be present in form of stellar-mass black holes in the inner tenths of a parsec. These higher estimates are probably due to the stellar mass function assumed by Morris (1993), which contain a larger fraction of stellar black hole progenitors.

The publications cited above considered mainly inflow of heavy stellar remnants from the inner bulge over the life time of the Galaxy, starting from an initially present stellar population with a given IMF. They did not consider possibly continually on-going star formation in the GC. Figer et al. (2004) infer a star formation rate of about $4 \times 10^{-7} M_\odot \text{ yr}^{-1} \text{ pc}^{-3}$ in the inner 50 pc of the GC. Under the assumption that this star formation rate is a typical value and has been largely constant over the life time of the Milky Way, this corresponds to a total mass of stars of $1.7 \times 10^7 M_\odot$ formed in the inner 10 pc over 10^{10} yr . Of course, a large fraction of the mass bound in stars will be returned to the ISM. The lighter stellar remnants may be pushed outward by mass segregation. However, if we assume that stars heavier than $30 M_\odot$ form stellar mass black holes of $7 M_\odot$ (see Miralda-Escudé & Gould 2000), then $\sim 1.2 \times 10^6 M_\odot$ will be locked in stellar-mass black holes. Here, we have assumed an IMF of the form $N(m) \propto m^{-1.3}$ and an upper mass cut-off of $120 M_\odot$ (choosing $80 M_\odot$ will give a very similar result).

We also have to consider the star formation that takes place in the inner 0.5 pc. Paumard et al. (2006) estimate a mass of $\sim 10^4 M_\odot$ for the young stars that formed in the most recent star burst event(s). There is evidence for another star formation event 10^8 yr ago (see Krabbe et al. 1995). If these values are typical, then we obtain a star formation rate of $10^{-4} M_\odot \text{ yr}^{-1}$ for the central half parsec. With the same assumptions used above, this leads to roughly $7 \times 10^5 M_\odot$ locked in stellar-mass black holes. Since the IMF in the central parsec appears to be top-heavy (Nayakshin & Sunyaev 2005; Paumard et al. 2006), the efficiency of producing black holes may be considerably higher in the GC. Note the dynamical upper limit on the number of stellar-mass black hole that can be packed into the central 0.5 pc for 10 Gyr while avoiding kicking each other into the MBH (the "drain limit" Alexander & Livio 2004) is not much larger, $\sim 2 \times 10^5$.

The considerations above are certainly very rough estimates, but show that it is not unreasonable to assume that a large number of dark stellar remnants may be present in the central parsecs of the GC. In fact, Muno et al. (2005) have found evidence that X-ray transients are overabundant by a factor of $\gtrsim 20$ per unit stellar mass in the central parsec. If a significant fraction of these transients is related to stellar mass black holes, this may explain the excess in non-stellar mass in the GC cluster. There are also contradictory studies. Deegan & Nayakshin (2006) conclude from considerations concerning the diffuse X-ray emission from the central parsec that not more than 20,000 stellar-mass BHs can be present in this region. Clearly, the issue needs further intensive study. Here, we mainly want to make the point that stellar dynamics shows that the amount of mass in the extended stellar cluster appears to be much larger than what could be explained by stars alone. Stellar remnants may be a possibility to explain this discrepancy. A large number of stellar remnants would have important implications on physical mechanisms such as gravitational lensing of background stars, and destruction and scattering of stars in the central parsec (see, e.g., Morris 1993; Alexander 2001, 2005).

5. Summary

In this work, we have presented seeing limited and AO assisted high-resolution NIR imaging observations of the stellar cluster in the central parsec of the GC. The data were used to extract information on the stellar number density and on the diffuse background light density in the GC. Both star counts and background light density were corrected for crowding effects and interstellar extinction in the GC. A detailed map of the variation of the interstellar extinction in the central parsec of the Milky Way was presented. We compared our analysis to theoretical expectations. Our results are summarised in the following points:

1. The overall structure of the GC nuclear cluster can be described well by a broken power-law as found already by Genzel et al. (2003b). A single-power-law is clearly insufficient to describe the cluster structure.
2. From the different data sets and methods (background light, number counts), we have derived various estimates of the inner and outer power-law indices and of the break radius. The different estimates agree well within their uncertainties. From their comparison, we derive a power-law index of $\Gamma = 0.19 \pm 0.05$ for the cusp, a power-law index of $\Gamma = 0.75 \pm 0.1$ for the outer part of the cluster, and a break radius of $R_{\text{break}} = 6.0 \pm 1.0''$ or $0.22 \pm 0.04 \text{ pc}$ (the power-law indices refer to the measured *projected* density). The cusp appears flatter than what is predicted by most theoretical work. This may be related to a very high density of the stellar cluster.
3. The best available measurements of the velocity dispersion of the cluster from the literature are used in order to derive the enclosed mass/mass density vs. distance from Sgr A*. We obtain significantly higher mass estimates for the central parsec than previously considered. The inferred density of the extended mass at the break radius is $2.8 \pm 1.3 \times 10^6 M_\odot \text{ pc}^{-3}$. The inferred high mass of the cluster agrees very well with the extent of the cusp, assuming that the cusp extends to $0.1 - 0.2 r_h$, where r_h is the radius around Sgr A* within which the cluster contains twice the mass of the supermassive black hole. We find that the mass of the stars in the cluster may only represent about 50% percent of the actually present mass in the cluster within the central pc. The work of other authors and some rough estimates in this work show that stellar-mass black holes may contribute a large part of the dark mass.
4. The examination of the stellar surface density for different magnitude bins reveals a trend in the spatial distribution that could be the result of mass segregation. The horizontal branch stars, with K-magnitudes around 15.25, are in their majority horizontal branch/red clump stars that are expected to trace the old, relaxed stellar population. They have the lowest mean mass of all observed stars in our images and, consistent with theoretical expectations, the flattest power-law index inside the cusp. We also find that there exists either an under-density of HB/RC stars around $R = 5''$, or, alternatively, an over-density of similarly bright stars at $R = 3''$ and $R = 7''$.

5. Several density clumps appear to be present in the cluster, especially at projected distances of $3''$ and $7''$ from Sgr A*. Their nature is unclear, but they may be related to the recent star formation events.
6. A detailed map of the variation of interstellar extinction in the central ~ 0.5 pc of the Milky Way is presented. Extinction is highly variable and has a general minimum centred on Sgr A* and in a strip running NE-SW across Sgr A*. The extinction map in combination with possible shock structures in an L'-band map may provide some support to the assumption of an (aligned) outflow from the central arc seconds.

Acknowledgements. Part of this work was supported by the German *Deutsche Forschungsgemeinschaft*, DFG project number SFB 494 and by the DFG Schwerpunktprogramm SPP1177. TA was supported by ISF grant 928/06, Minerva grant 8563, and a New Faculty grant by Sir H. Djangoly, CBE, of London, UK. DM was supported by grants AST-0437519 from the NSF and NNG04GJ48G from NASA.

References

- Alexander, T. 1999, *ApJ*, 527, 835
 Alexander, T. 2001, *ApJ*, 553, L149
 Alexander, T. 2005, *Phys. Rep.*, 419, 65
 Alexander, T. & Livio, M. 2004, *ApJ*, 606, L21
 Alexander, T. & Sternberg, A. 1999, *ApJ*, 520, 137
 Allen, D. A., Hyland, A. R., & Hillier, D. J. 1990, *MNRAS*, 244, 706
 Amaro-Seoane, P., Freitag, M., & Spurzem, R. 2004, *MNRAS*, 352, 655
 Bahcall, J. N. & Tremaine, S. 1981, *ApJ*, 244, 805
 Bahcall, J. N. & Wolf, R. A. 1976, *ApJ*, 209, 214
 Bahcall, J. N. & Wolf, R. A. 1977, *ApJ*, 216, 883
 Becklin, E. E. & Neugebauer, G. 1968, *ApJ*, 151, 145
 Bergström, L., Fairbairn, M., & Pieri, L. 2006, *Phys. Rev. D*, 74, 123515
 Blandford, R. D. & Begelman, M. C. 1999, *MNRAS*, 303, L1
 Blum, R. D., Sellgren, K., & Depoy, D. L. 1996, *ApJ*, 470, 864
 Bower, G. C., Falcke, H., Herrnstein, R. M., et al. 2004, *Science*, 304, 704
 Catchpole, R. M., Whitelock, P. A., & Glass, I. S. 1990, *MNRAS*, 247, 479
 Christopher, M. H., Scoville, N. Z., Stolovy, S. R., & Yun, M. S. 2005, *ApJ*, 622, 346
 Clénet, Y., Rouan, D., Gratadour, D., et al. 2004, *A&A*, 424, L21
 Deegan, P. & Nayakshin, S. 2006, *Journal of Physics Conference Series*, 54, 306
 Diolaiti, E., Bendinelli, O., Bonaccini, D., et al. 2000, *A&AS*, 147, 335
 Draine, B. T. 1989, *Interstellar extinction in the infrared (Infrared Spectroscopy in Astronomy, Proceedings of the 22nd Eslab Symposium held in Salamanca, Spain, 7-9 December, 1988. Edited by B.H. Kaldeich. ESA SP-290. European Space Agency, 1989., p.93), 93–+*
 Eckart, A., Baganoff, F. K., Schödel, R., et al. 2006a, *A&A*, 450, 535
 Eckart, A. & Genzel, R. 1996, *Nature*, 383, 415
 Eckart, A., Genzel, R., Hofmann, R., Sams, B. J., & Tacconi-Garman, L. E. 1993, *ApJ*, 407, L77
 Eckart, A., Genzel, R., Hofmann, R., Sams, B. J., & Tacconi-Garman, L. E. 1995, *ApJ*, 445, L23
 Eckart, A., Schödel, R., Meyer, L., et al. 2006b, *A&A*, 455, 1
 Efron, B. 1982, *The Jackknife, the Bootstrap and other resampling plans (CBMS-NSF Regional Conference Series in Applied Mathematics, Philadelphia: Society for Industrial and Applied Mathematics (SIAM), 1982)*
 Eisenhauer, F., Genzel, R., Alexander, T., et al. 2005, *ApJ*
 Eisenhauer, F., Schödel, R., Genzel, R., et al. 2003, *ApJ*, 597, L121
 Figer, D. F., Gilmore, D., Kim, S. S., et al. 2003, *ApJ*, 599, 1139
 Figer, D. F., Rich, R. M., Kim, S. S., Morris, M., & Serabyn, E. 2004, *ApJ*, 601, 319
 Freitag, M., Amaro-Seoane, P., & Kalogera, V. 2006, *ApJ*, 649, 91
 Genzel, R., Pichon, C., Eckart, A., Gerhard, O. E., & Ott, T. 2000, *MNRAS*, 317, 348
 Genzel, R., Schödel, R., Ott, T., et al. 2003a, *Nature*, 425, 934
 Genzel, R., Schödel, R., Ott, T., et al. 2003b, *ApJ*, 594, 812
 Genzel, R., Thatte, N., Krabbe, A., Kroker, H., & Tacconi-Garman, L. E. 1996, *ApJ*, 472, 153
 Ghez, A. M., Duchêne, G., Matthews, K., et al. 2003, *ApJ*, 586, L127
 Ghez, A. M., Morris, M., Becklin, E. E., Tanner, A., & Kremenek, T. 2000, *Nature*, 407, 349
 Ghez, A. M., Wright, S. A., Matthews, K., et al. 2004, *ApJ*, 601, L159
 Girardi, L., Bressan, A., Bertelli, G., & Chiosi, C. 2000, *A&AS*, 141, 371
 Guesten, R., Genzel, R., Wright, M. C. H., et al. 1987, *ApJ*, 318, 124
 Haller, J. W., Rieke, M. J., Rieke, G. H., et al. 1996, *ApJ*, 456, 194
 Hopman, C. & Alexander, T. 2006, *ApJ*, 645, L133
 Jackson, J. M., Geis, N., Genzel, R., et al. 1993, *ApJ*, 402, 173
 Kent, S. M. 1992, *ApJ*, 387, 181
 Krabbe, A., Genzel, R., Eckart, A., et al. 1995, *ApJ*, 447, L95
 Launhardt, R., Zylka, R., & Mezger, P. G. 2002, *A&A*, 384, 112
 Lee, M. H. & Goodman, J. 1989, *ApJ*, 343, 594
 Levin, Y. & Beloborodov, A. M. 2003, *ApJ*, 590, L33
 Lightman, A. P. & Shapiro, S. L. 1977, *ApJ*, 211, 244
 Lutz, D., Krabbe, A., & Genzel, R. 1993, *ApJ*, 418, 244
 Maillard, J. P., Paumard, T., Stolovy, S. R., & Rigaut, F. 2004, *A&A*, 423, 155
 Markoff, S., Falcke, H., & Fender, R. 2001, *A&A*, 372, L25
 Melia, F., Coker, R. F., & Yusef-Zadeh, F. 1996, *ApJ*, 460, L33+
 Melia, F. & Falcke, H. 2001, *ARA&A*, 39, 309
 Merritt, D. 2006, *Reports of Progress in Physics*, 69, 2513
 Merritt, D. & Szell, A. 2006, *ApJ*, 648, 890
 Merritt, D. & Tremblay, B. 1994, *AJ*, 108, 514
 Meyer, L., Eckart, A., Schödel, R., et al. 2006a, *A&A*, 460, 15
 Meyer, L., Schödel, R., Eckart, A., et al. 2006b, *A&A*, 458, L25
 Miller, G. E. & Scalo, J. M. 1979, *ApJS*, 41, 513

- Miralda-Escudé, J. & Gould, A. 2000, *ApJ*, 545, 847
- Morris, M. 1993, *ApJ*, 408, 496
- Mouawad, N., Eckart, A., Pfalzner, S., et al. 2005, *Astronomische Nachrichten*, 326, 83
- Moultaka, J., Eckart, A., Schödel, R., Viehmann, T., & Najarro, F. 2005, *A&A*, 443, 163
- Muno, M. P., Bauer, F. E., Bandyopadhyay, R. M., & Wang, Q. D. 2006, *ApJS*, 165, 173
- Muno, M. P., Pfahl, E., Baganoff, F. K., et al. 2005, *ApJ*, 622, L113
- Murphy, B. W., Cohn, H. N., & Durisen, R. H. 1991, *ApJ*, 370, 60
- Navarro, J. F., Frenk, C. S., & White, S. D. M. 1996, *ApJ*, 462, 563
- Nayakshin, S. 2006, *MNRAS*, 372, 143
- Nayakshin, S., Dehnen, W., Cuadra, J., & Genzel, R. 2006, *MNRAS*, 366, 1410
- Nayakshin, S. & Sunyaev, R. 2005, *MNRAS*, 364, L23
- Ott, T. 2004, Ph.D. Thesis
- Ott, T., Eckart, A., & Genzel, R. 1999, *ApJ*, 523, 248
- Paumard, T., Genzel, R., Martins, F., et al. 2006, *ApJ*, 643, 1011
- Philipp, S., Zylka, R., Mezger, P. G., et al. 1999, *A&A*, 348, 768
- Preto, M., Merritt, D., & Spurzem, R. 2004, *ApJ*, 613, L109
- Quataert, E. 2003, *Astronomische Nachrichten Supplement*, 324, 435
- Quinlan, G. D., Hernquist, L., & Sigurdsson, S. 1995, *ApJ*, 440, 554
- Reid, M. J. 1993, *ARA&A*, 31, 345
- Reid, M. J., Menten, K. M., Genzel, R., et al. 2003, *ApJ*, 587, 208
- Rieke, G. H. & Rieke, M. J. 1988, *ApJ*, 330, L33
- Schödel, R., Ott, T., Genzel, R., et al. 2003, *ApJ*, 596, 1015
- Schödel, R., Ott, T., Genzel, R., et al. 2002, *Nature*, 419, 694
- Schaller, G., Schaerer, D., Meynet, G., & Maeder, A. 1992, *A&AS*, 96, 269
- Schödel, R., Eckart, A., Iserlohe, C., Genzel, R., & Ott, T. 2005, *ApJ*, 625, L111
- Scott, D. W. 1992, *Multivariate Density Estimation* (Multivariate Density Estimation, Wiley, New York, 1992)
- Scoville, N. Z., Stolovy, S. R., Rieke, M., Christopher, M., & Yusef-Zadeh, F. 2003, *ApJ*, 594, 294
- Spitzer, L. 1987, *Dynamical evolution of globular clusters* (Princeton, NJ, Princeton University Press, 1987, 191 p.)
- Tripp, S., Paumard, T., Ott, T., et al. 2006, *ArXiv Astrophysics e-prints*
- Warwick, R., Sakano, M., & Decourchelle, A. 2006, *Journal of Physics Conference Series*, 54, 103
- Young, P. 1980, *ApJ*, 242, 1232
- Yuan, F., Markoff, S., & Falcke, H. 2002, *A&A*, 383, 854
- Yusef-Zadeh, F., Roberts, D. A., & Biretta, J. 1998, *ApJ*, 499, L159

Table 1. Details of the ISAAC/VLT observations used for this work. DIT is the detector integration time. NDIT is the number of integrations that were averaged online by the read-out electronics. N is the number of exposures that were taken. The total integration time amounts to $N \times \text{NDIT} \times \text{DIT}$. FWHM is the approximate full width at half maximum of the PSF due to seeing. The pixel scale was $0.147''$ per pixel.

Date	$\lambda_{\text{central}} [\mu\text{m}]$	$\Delta\lambda [\mu\text{m}]$	N	NDIT	DIT [sec]	FWHM
02 July 1999	1.25	0.29	6	12	24.0	$0.4''$
02 July 1999	2.09	0.02	6	12	24.0	$0.4''$
27 July 2005	1.65	0.30	8	5	1.8	$0.9''$

Table 2. Details of the NACO/VLT observations used for this work. DIT is the detector integration time. NDIT is the number of integrations that were averaged online by the read-out electronics. N is the number of exposures that were taken. The total integration time amounts to $N \times \text{NDIT} \times \text{DIT}$. The pixel scale of all observations was $0.027''$ per pixel.

Date	$\lambda_{\text{central}} [\mu\text{m}]$	$\Delta\lambda [\mu\text{m}]$	N	NDIT	DIT [sec]
12 June 2004	2.06	0.06	96	1	30
12 June 2004	2.24	0.06	99	1	30
9 July 2004	2.00	0.06	8	4	36
9 July 2004	2.24	0.06	8	4	36
9 July 2004	2.27	0.06	8	4	36
9 July 2004	2.30	0.06	8	4	36

Table 3. Completeness of stars detected in the ISAAC $2.09 \mu\text{m}$ image. R is the projected distance from Sgr A*.

mag _K	$R < 60''$	$15'' < R < 60''$	$R < 15''$
12	99%	99%	98%
13	99%	99%	93%
14	95%	97%	80%
15	87%	89%	53%
16	63%	66%	16%
17	22%	23%	1%

Table 4. Completeness of stars detected in the NACO $2.27 + 2.30 \mu\text{m}$ image. R is the projected distance from Sgr A*.

mag _K	$R < 8''$	$R > 8''$
14	97.1%	98.7%
15	93.5%	96.9%
16	84.4%	91.6%
17	65.1%	77.8%

Table 5. Break radius and power-law indices for the central stellar cluster.

method	R_{break}	Γ_{cusp}	Γ_{cluster}
counts ^a _{ISAAC}	-	-	0.68 ± 0.02
background ^b _{ISAAC}	6.5 ± 1.1	0.2 ± 0.11	0.95 ± 0.11
counts ^c _{NACO}	6.75 ± 0.5	0.30 ± 0.05	0.55 ± 0.05
background ^d _{NACO}	4.0 ± 0.8	0.15 ± 0.07	0.85 ± 0.1
counts ^e _{NACO,HB}	5.75 ± 0.5	0.10 ± 0.05	0.75 ± 0.05
	6.0 ± 1.0	0.19 ± 0.05	0.75 ± 0.10

^a star counts on ISAAC image (see Fig. 4 and section 3.1.2)

^b diffuse background on ISAAC image (see Fig. 5 and section 3.1.3); uncertainties based on formal fit error and tests with artificial background

^c star counts on NACO image (see Fig. 12 and section 3.2.6)

^d diffuse background on NACO image (see Fig. 14 and section 3.2.7)

^e star counts on NACO image, brightness range of HB/RC stars (see Fig. 17 and section 4.2)

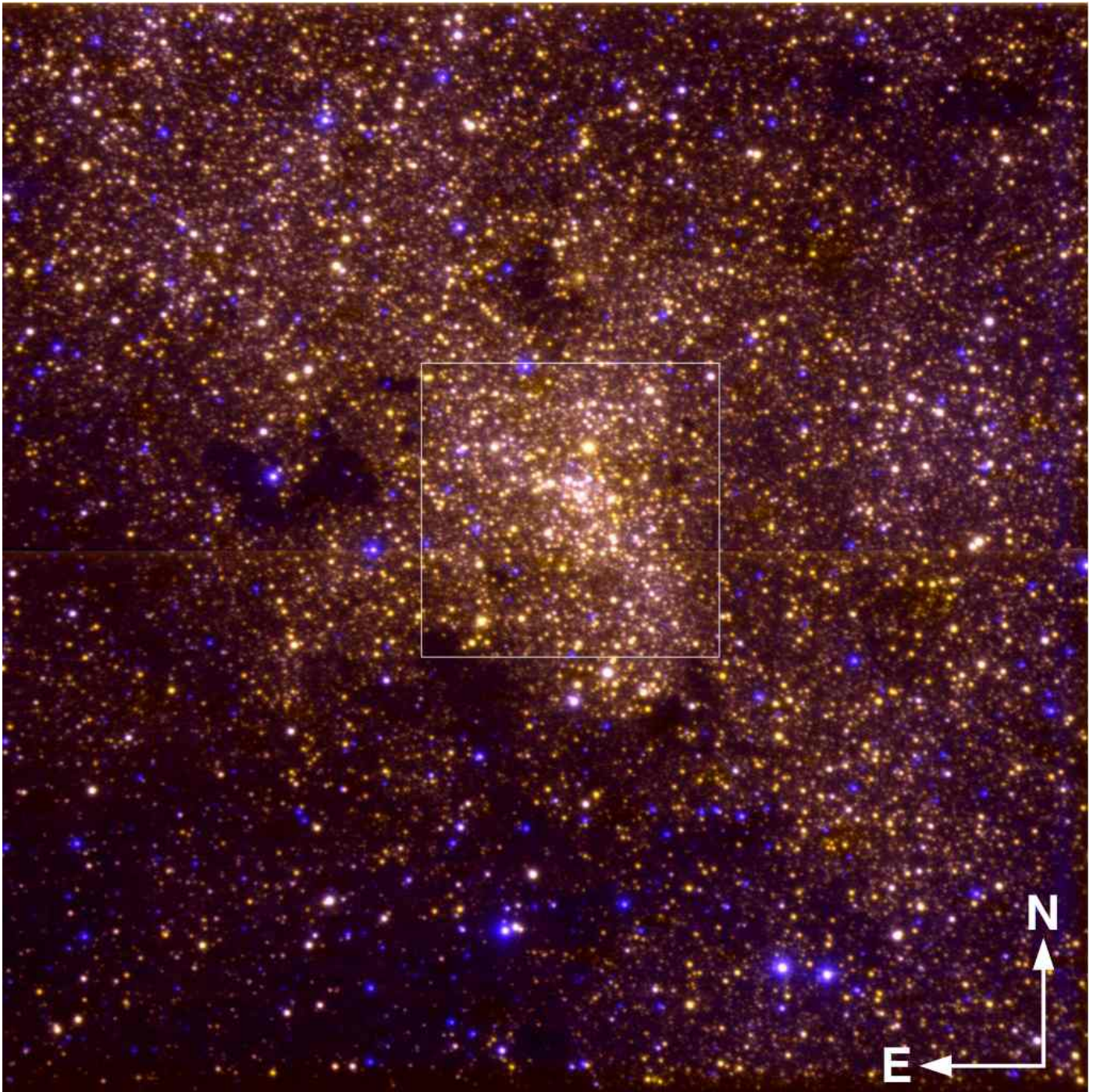


Fig. 1. Colour image composed of ISAAC imaging observations at $2.09\,\mu\text{m}$ and in the J-band. The field-of-view is $150'' \times 150''$. The field of about $40'' \times 40''$ that was observed with AO observations is marked by a square. The galactic plane runs approximately southwest-northeast across the image. Blue sources are foreground stars. The patchy and highly variable extinction is evident, as well as the minimum of the extinction on the central cluster.

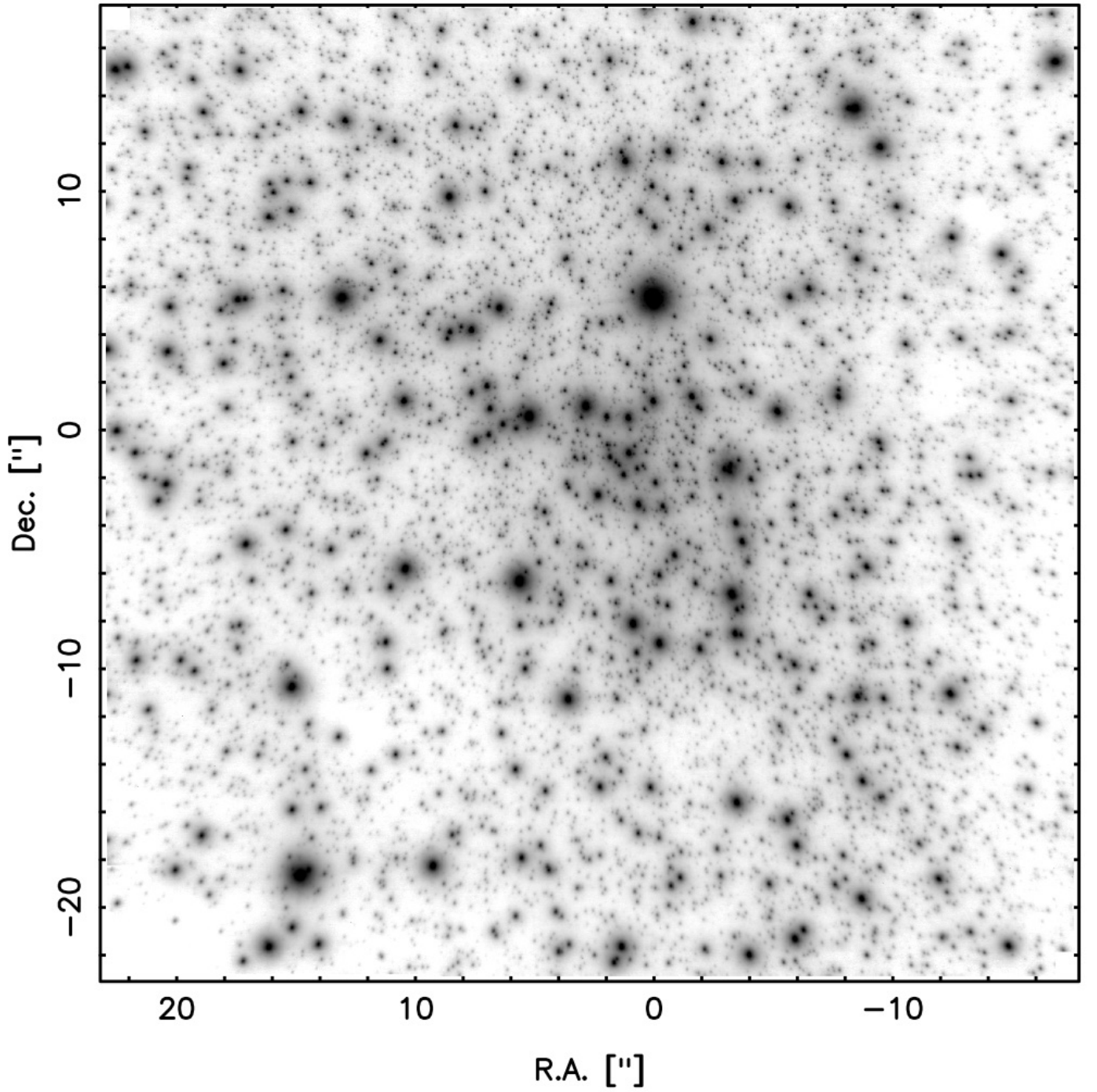


Fig. 2. Final mosaic of the $2.27 + 2.30 \mu\text{m}$ IB filter AO imaging data with the $0.027''$ pixel scale, centred on Sgr A*. The offsets from Sgr A* in right ascension and declination that are labelled on the coordinate axes serve as an orientation, but do not represent high accuracy astrometry because there may be a slight ($< 1^\circ$) remnant rotation present in the images. North is up and east is to the left.

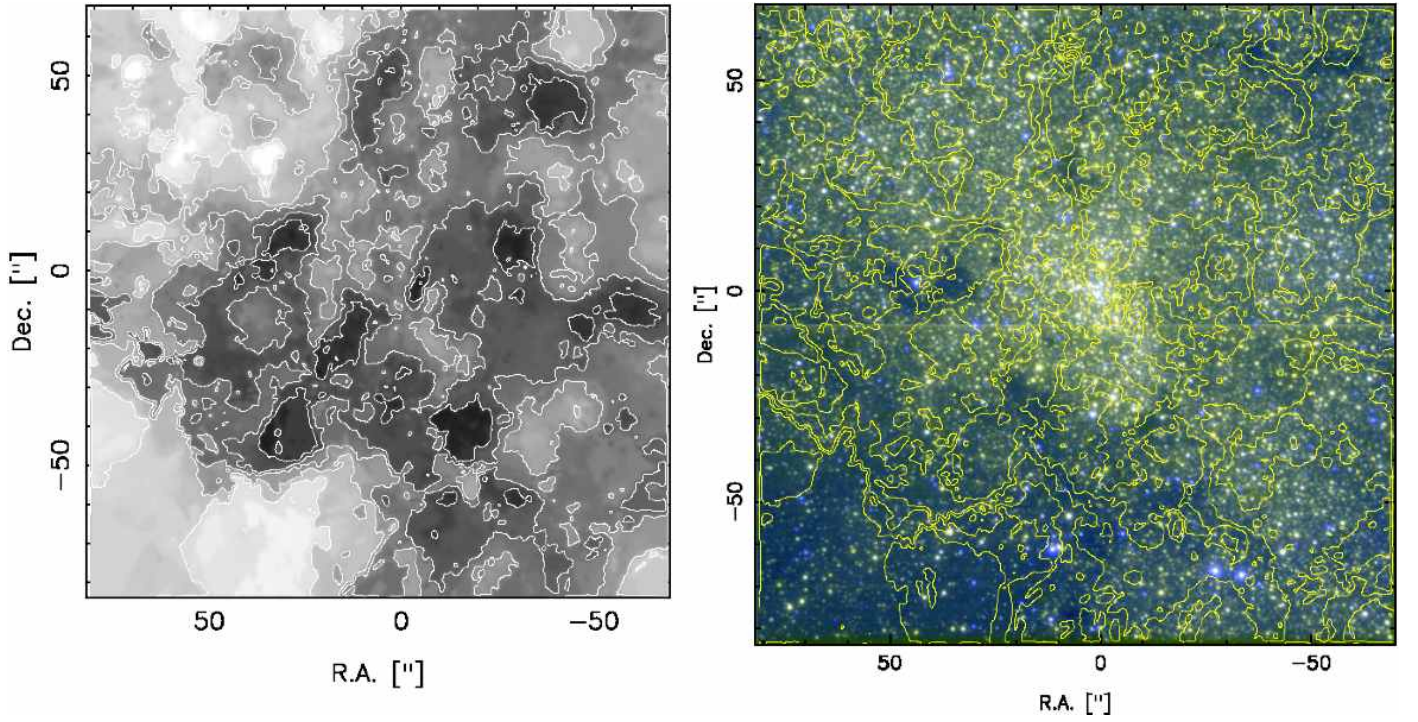


Fig. 3. Left: Extinction map derived from H-band and $2.09\,\mu\text{m}$ images of the central stellar cluster with ISAAC/VLT. The details of the method are described in the text. Contours are plotted from $A_K = 1.8 - 3.6$ in steps of $\Delta A_K = 0.3$. Darker shades correspond to higher extinction. Right: The extinction contours from the left panel are plotted over a combined J and K false colour image. Good agreement can be found between high extinction as seen by eye (darkness of regions, number of stars visible in regions) and the extinction contours. A stark discrepancy exists only in the south-western corner of the image. Here, extinction is so strong, that preferentially foreground stars contribute to the measurements, i.e. the extinction is underestimated.

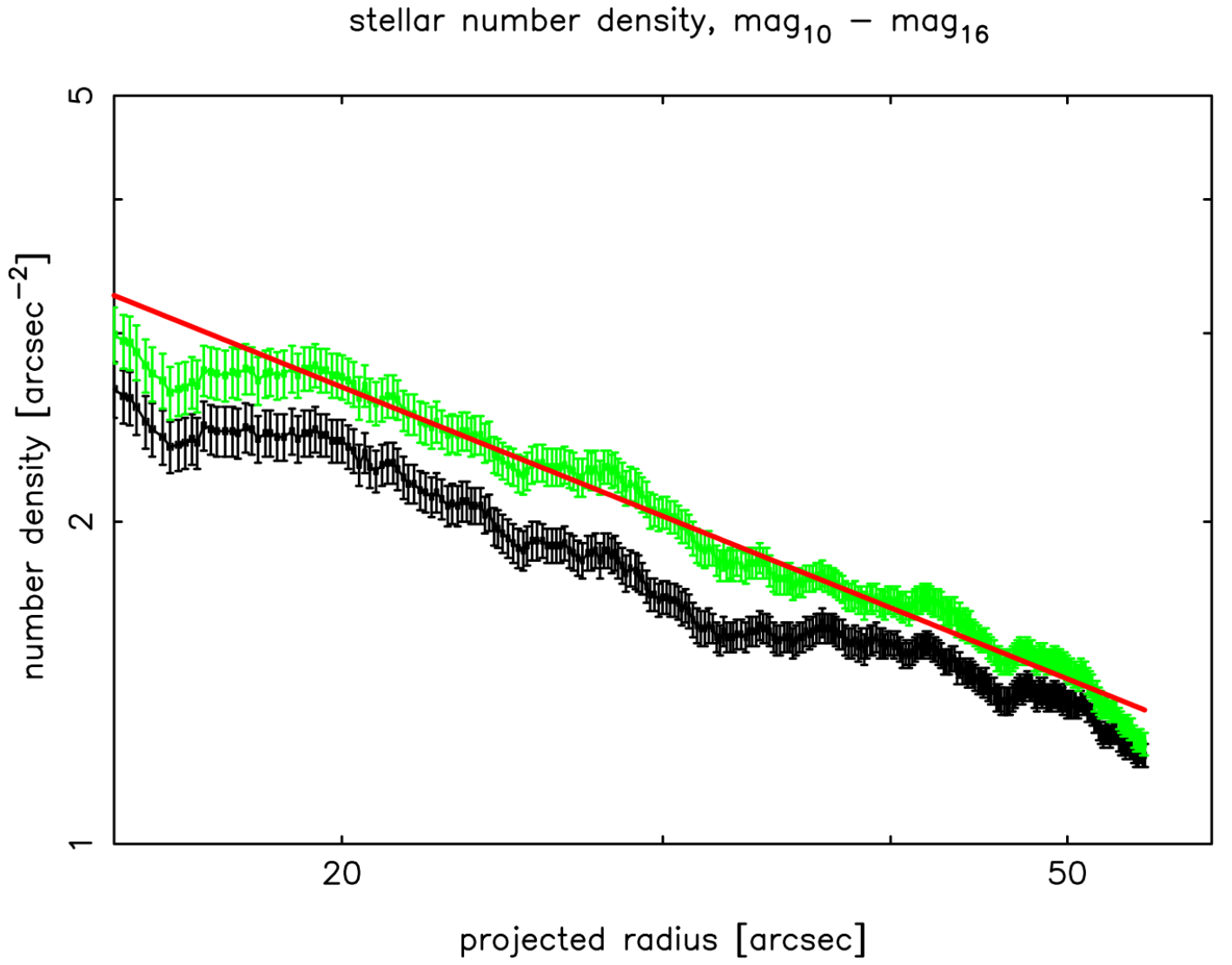


Fig. 4. Stellar number density extracted from ISAAC imaging observations at $2.09\,\mu\text{m}$ for $\text{mag}_K \leq 16$. The x-axis starts at $15''$. The lower, black data are completeness corrected counts, the upper green (grey) data have been additionally corrected for extinction. The straight line is a fit with a single power-law. It has an index of $\Gamma = 0.68 \pm 0.02$.

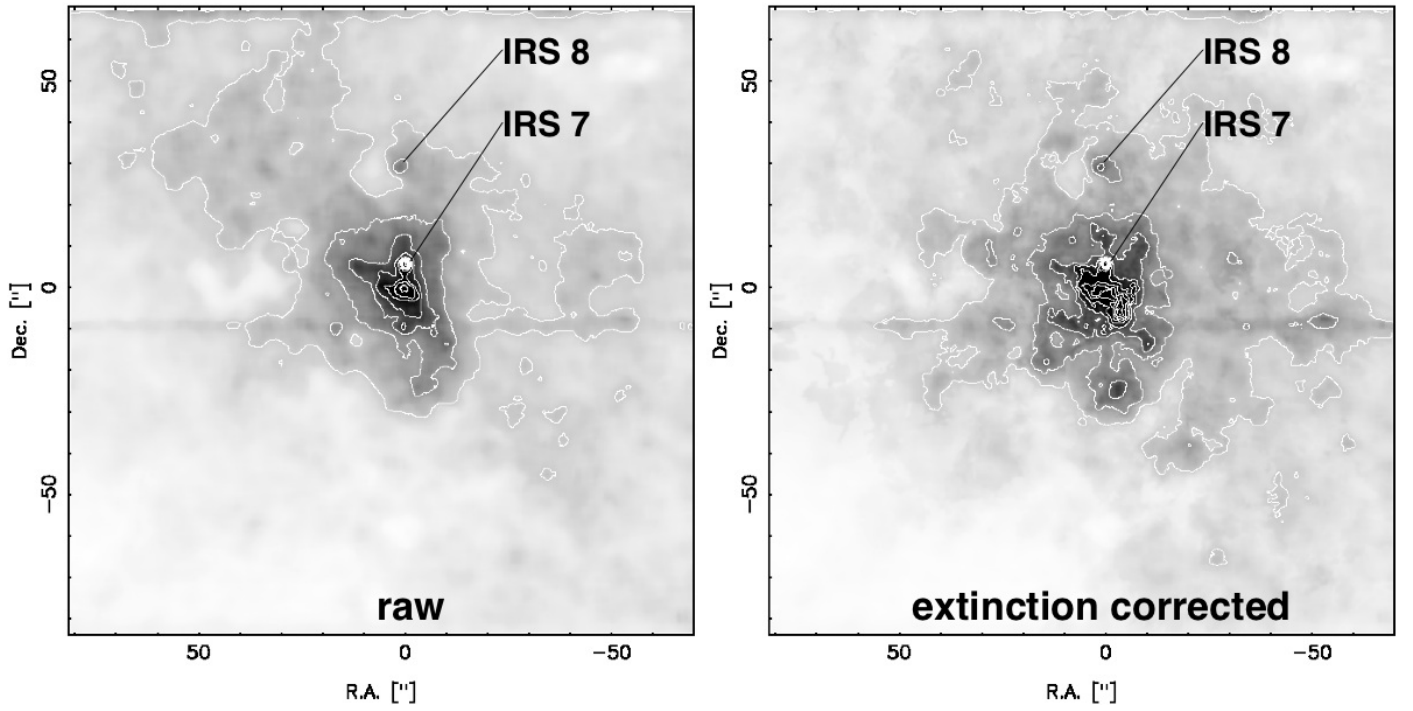


Fig. 5. Unresolved background light of the ISAAC $2.09\mu\text{m}$ image. Left: Raw, uncorrected background as extracted with the *StarFinder* code. Right: The background flux corrected for extinction (see Fig. 3). The horizontal line in both images is an artefact due to a detector artefact in the original image that could not be removed. The brightest star in the field, IRS 7, and the bright, extended source IRS 8 produced artefacts in the background light. Contour lines are plotted in steps of 10% from 10% to 100%, where 100% corresponds to the maximum flux in the image. Darker shades correspond to higher flux densities.

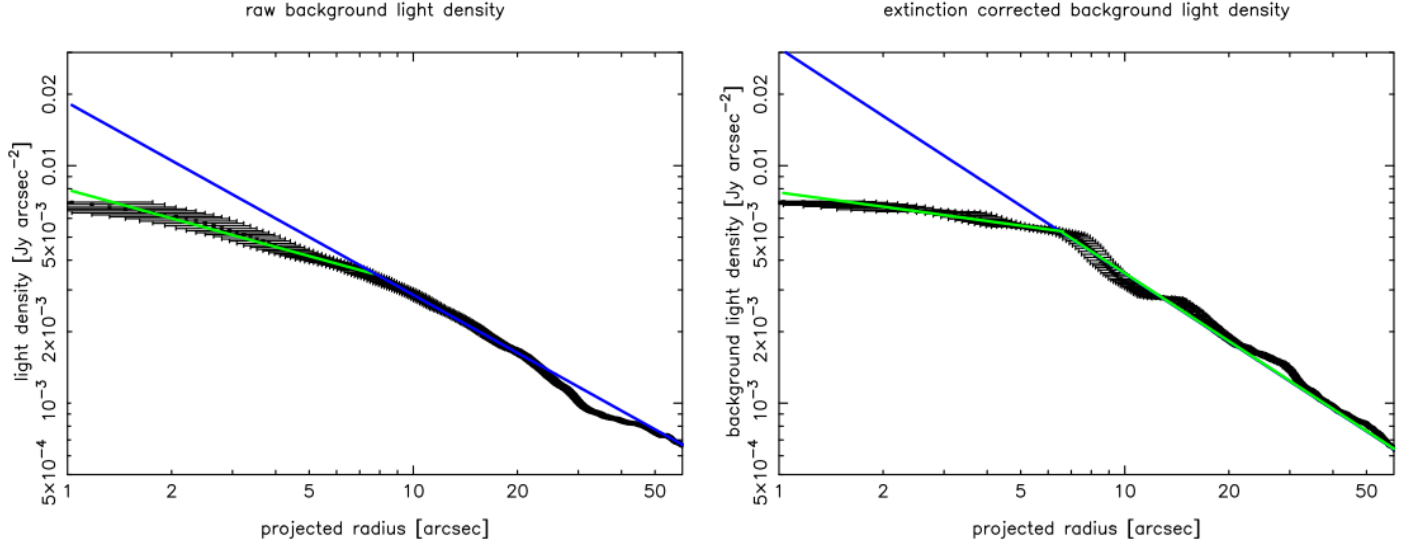


Fig. 6. Azimuthally averaged background light density in the ISAAC $2.09\,\mu\text{m}$ image. Left: Raw light density. Right: Extinction corrected light density. The units are counts/pixel. The straight lines indicate single and broken power law fits. The parameters of the fits are $\Gamma_{\text{cusp}} = 0.40 \pm 0.05$, $\Gamma_{\text{cluster}} = 0.8 \pm 0.02$, and $R_{\text{break}} = 7.5'' \pm 1.0''$ for the uncorrected light density. After correction for extinction, the best-fit values are $\Gamma_{\text{cusp}} = 0.2 \pm 0.05$, $\Gamma_{\text{cluster}} = 0.95 \pm 0.03$, and $R_{\text{break}} = 6.5'' \pm 0.5''$.

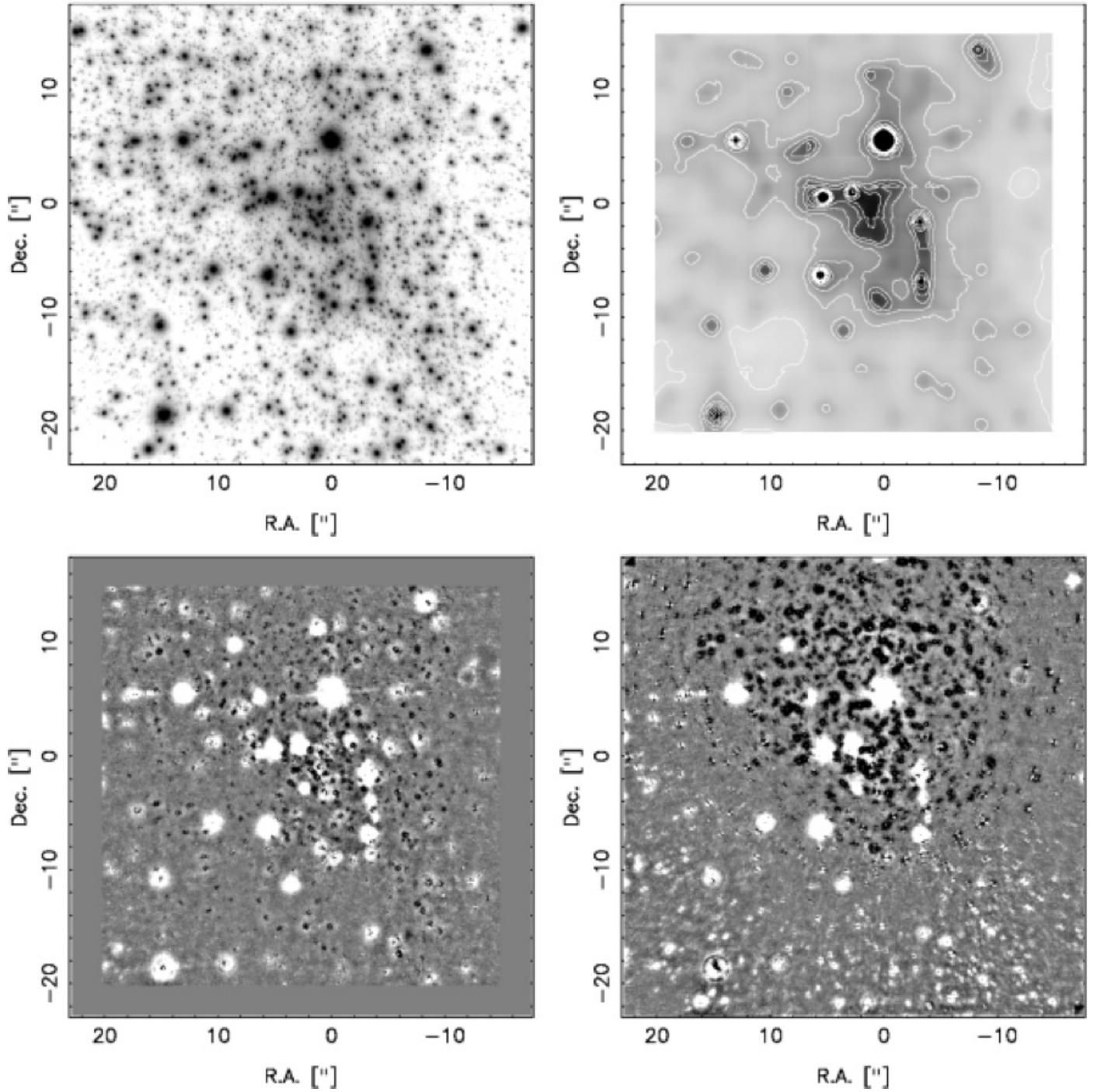


Fig. 7. Source extraction with *StarFinder* from AO images. This figure illustrates the influence of bright stars on the determination of the background and the effects of the spatially variable PSF. Upper left: original image ($2.27\,\mu\text{m}$). Upper right: Background estimated by *StarFinder*, using a spatially variable PSF. Darker shades correspond to higher flux densities. Lower left: Residual image when using a spatially variable PSF. Dark shades correspond to negative residuals. Lower right: Residual image when using a single PSF. Dark shades correspond to negative residuals.

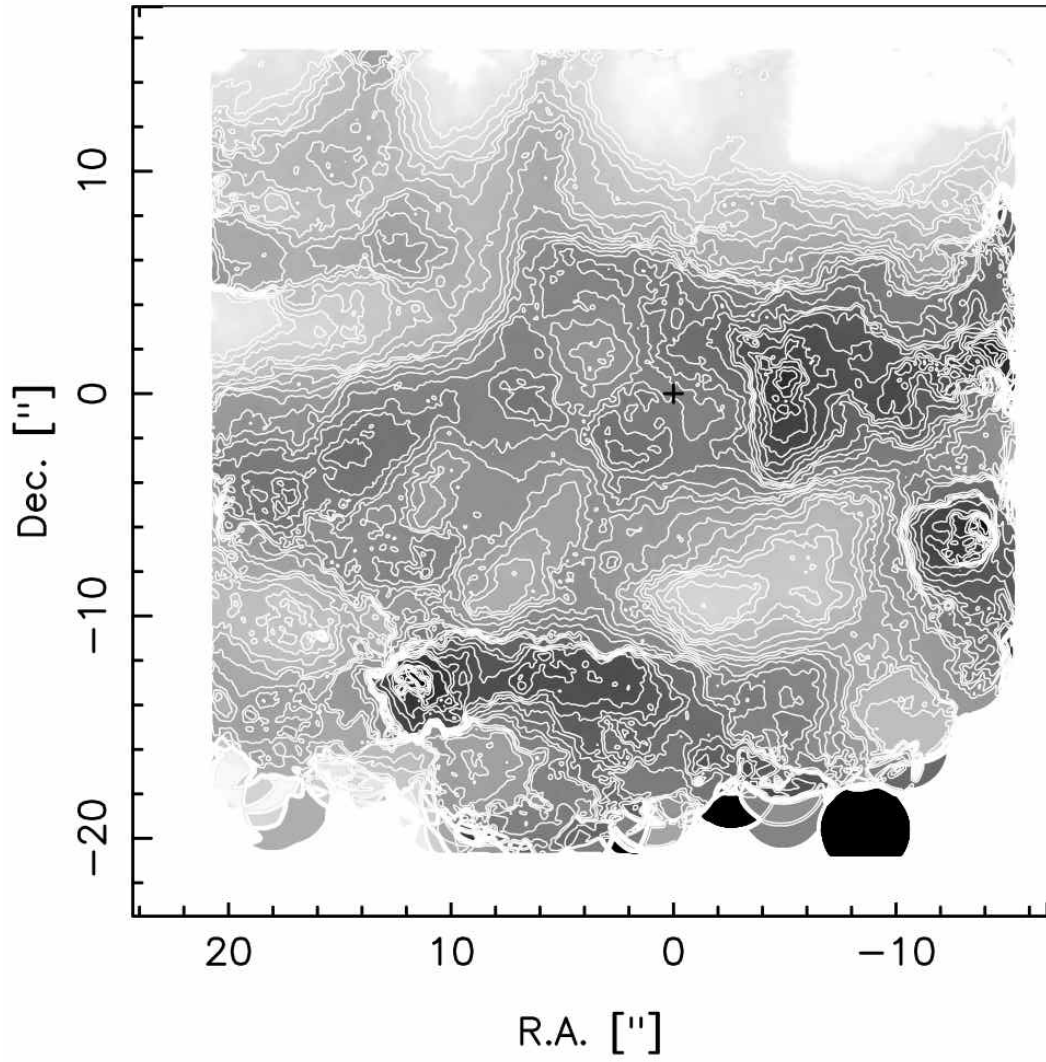


Fig. 8. Map of the interstellar extinction at $2.157\,\mu\text{m}$ derived from NACO intermediate band imaging. The contours are spaced from $A_{2.157\,\mu\text{m}} = 2.0 - 3.5$ mag at intervals of 0.05 mag. Darker shades correspond to higher extinction. The cross marks the position of Sgr A*, where $A_{2.157\,\mu\text{m}} = 2.6$ mag. The measurement at each pixel position results from the median of several tens of measurements within a projected distance of $2''$. The resolution of the extinction map is roughly $2''$.

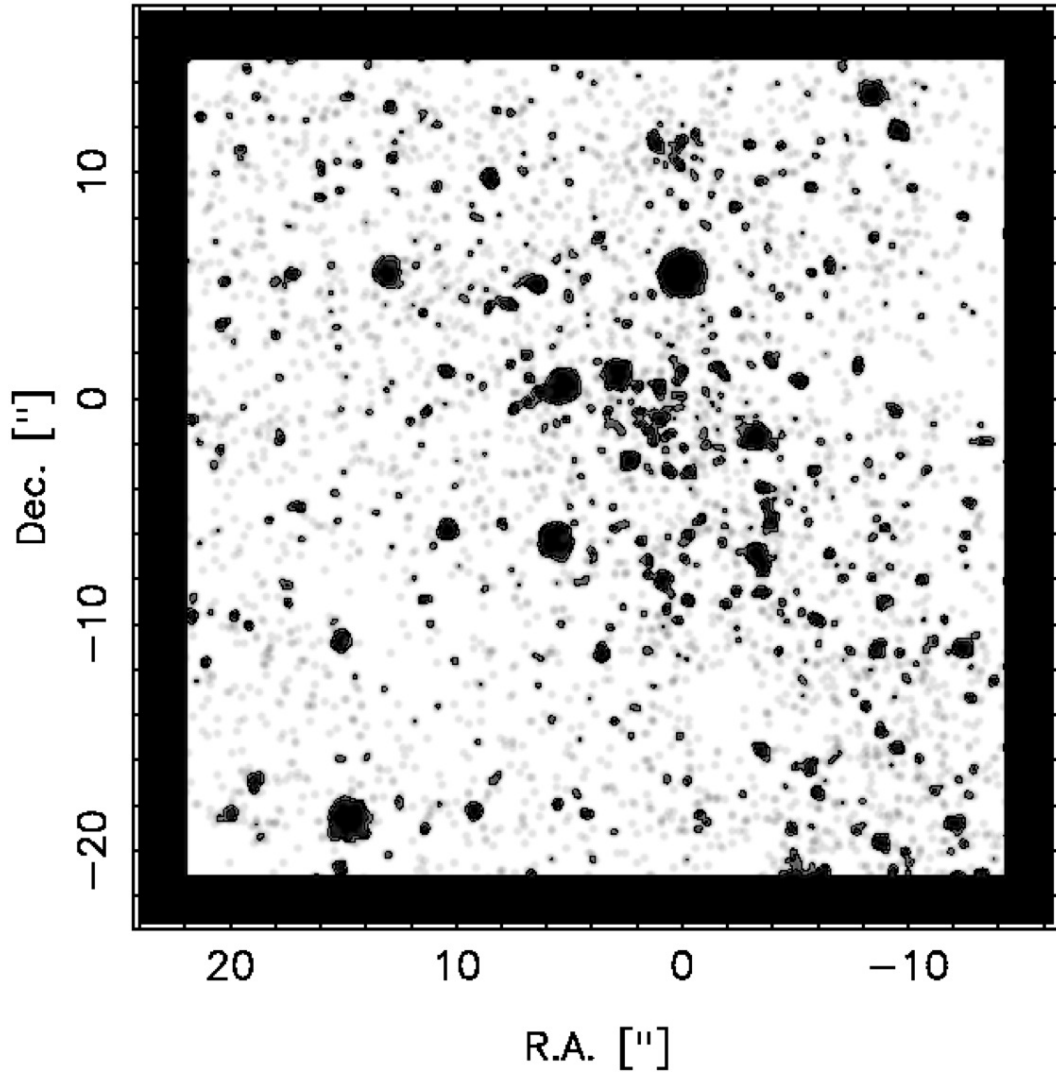


Fig. 9. Completeness map of the combined NACO $2.27 + 2.30\mu\text{m}$ image for $\text{mag}_K = 16$. Completeness increases from darker to lighter areas. Contours are plotted at 30% and 60% completeness.

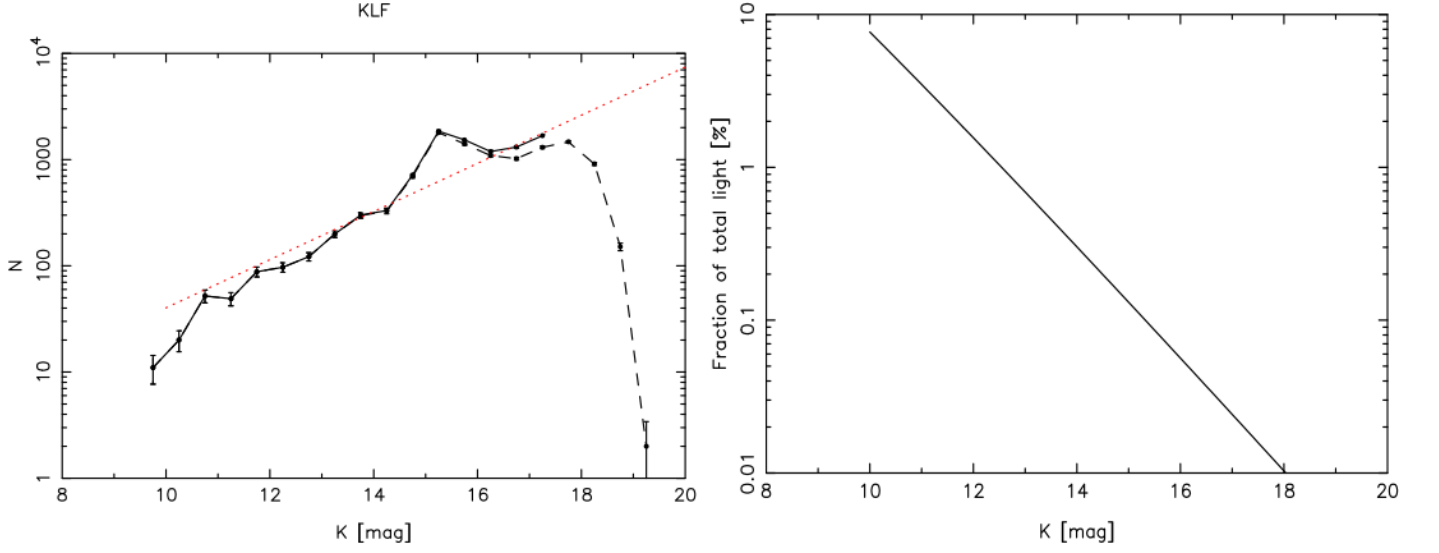


Fig. 10. The left panel shows the K-band luminosity function (KLF) of the GC stellar cluster as it was obtained from AO observations with NACO (field shown in Fig. 2). The dashed line indicates the raw counts, the straight line the completeness corrected counts. The 'bump' at $\text{mag}_K = 15.25$ is due to red clump/horizontal branch stars. The dotted line indicates a power law fit to the data – ignoring the red clump bump – with a power law index 0.23 ± 0.02 . The right panel illustrates the fraction of the total light of a star cluster that is contributed by stars of a given magnitude, under the assumption that the cluster LF is a pure power law. Here, the power law derived from the KLF in the panel above was used.

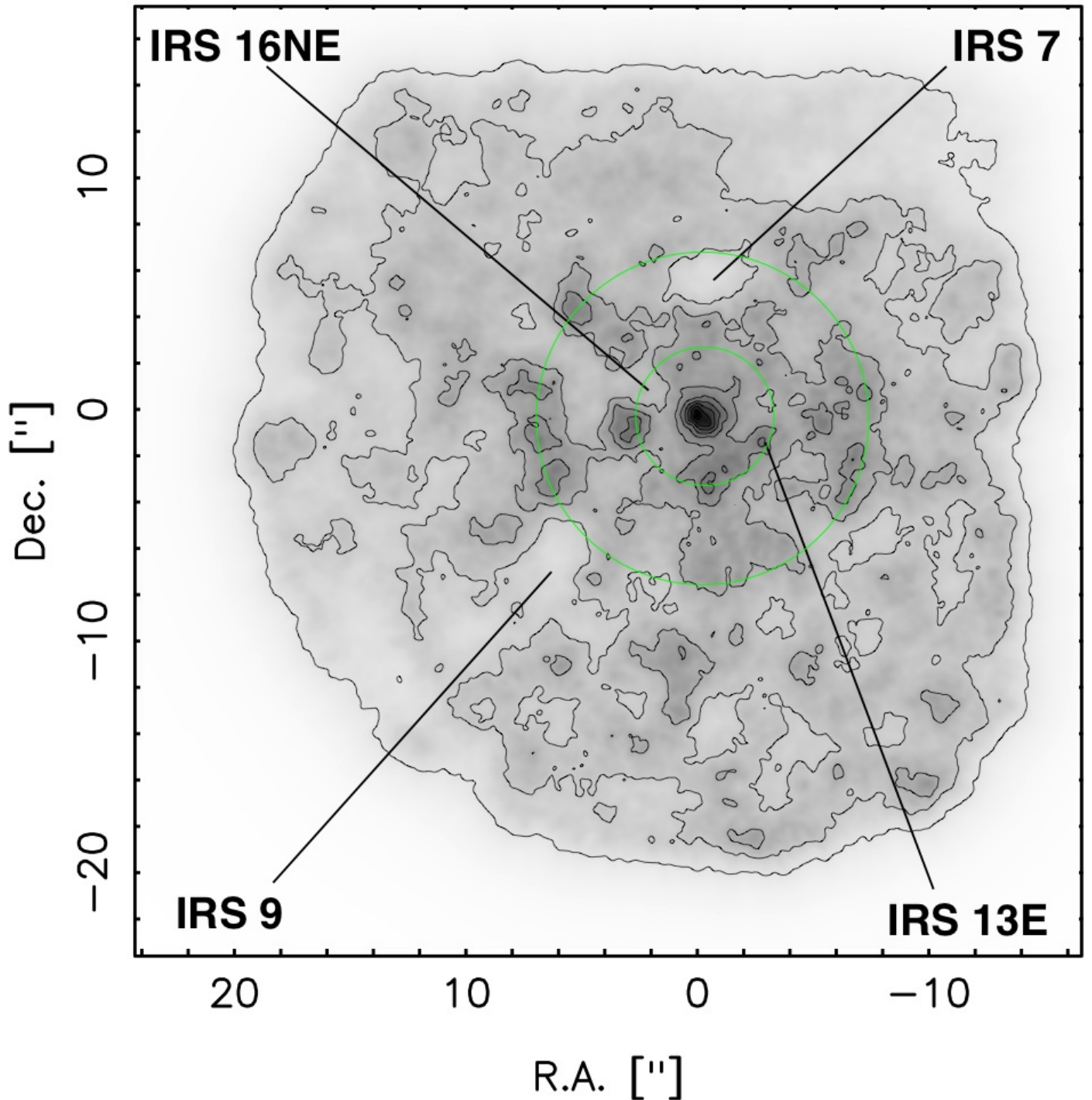


Fig. 11. Adaptively smoothed surface density map ($9.75 \leq \text{mag}_K \leq 17.75$) of the inner $\sim 20''$ of the GC stellar cluster. Contours are plotted in five steps of 0.67 times the maximum density. Darker shades correspond to higher surface densities. The adaptive smoothing was chosen such that 40 stars contributed to the density measurement at each pixel in the map. The resulting smoothing radius was $\sim 0.6''$ at distances $R < 1''$ from Sgr A*, $\sim 1''$ at $1'' < R < 10''$, and $\sim 1.2'' - 2''$ at $R > 10''$. The map was corrected for extinction and completeness. Since regions of completeness $< 30\%$ for given magnitudes were masked, the density near bright stars is under-estimated in this map. Some of these stars are indicated in the image. The masking is most probably the reason why the density peak is not centred on Sgr A* because of the bright star IRS 16NW located $\sim 1''$ north of Sgr A*. The green (light gray) rings indicate projected distances of $3''$ and $7''$ from Sgr A*. At these distances the structure of the cluster appears clumpy, with several density peaks superposed onto the generally smooth background. These structures are also present in the map before correction for extinction.

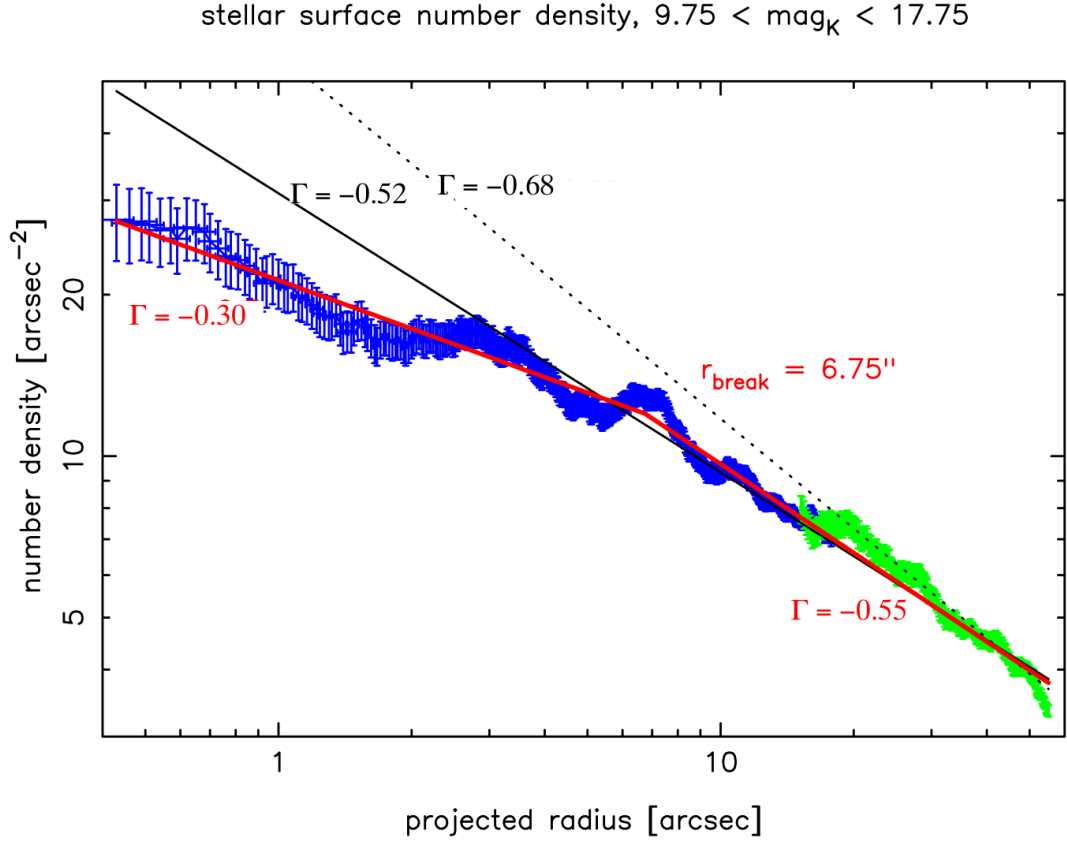


Fig. 12. Azimuthally averaged extinction and crowding corrected surface density vs. distance from Sgr A*. The green data points at large distances are from the ISAAC star counts (Fig. 4). They have been scaled to the NACO data (blue) by using the density in the overlapping region (The ISAAC data are less deep than the NACO data). Fits to the NACO data with a single (black) and with a broken (red) power-law are indicated along with the corresponding power-law indices. The ISAAC data were not used for the fits. The 1σ uncertainty of the power-law indices is 0.05 and of the break radius 0.05". The dotted line indicates the best-fit power-law for the ISAAC data (see Fig. 4).

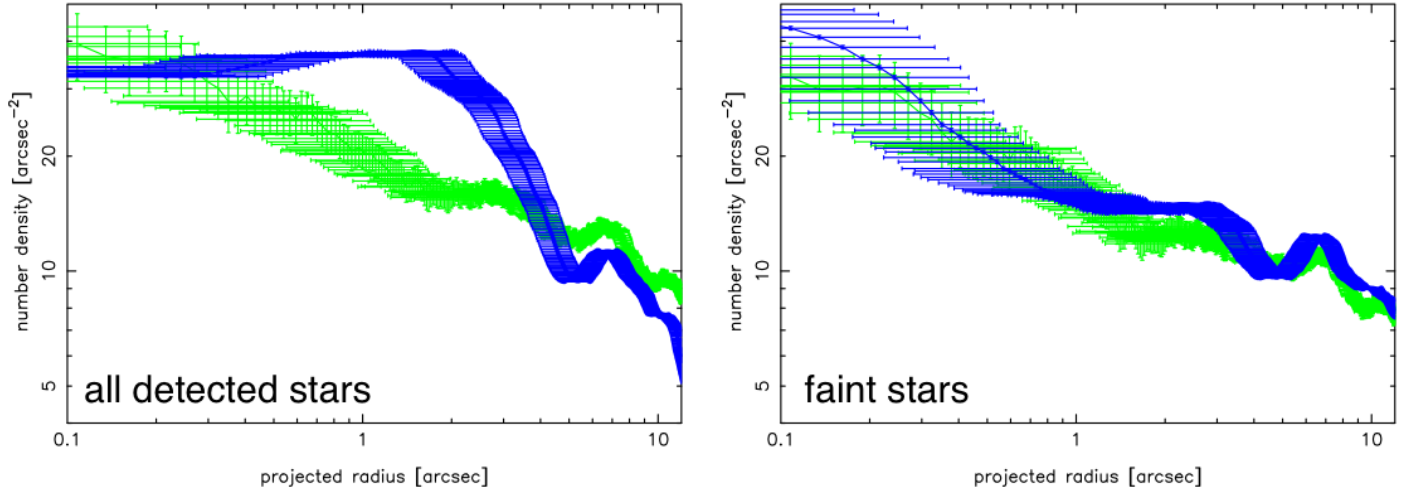


Fig. 13. Comparison between the extinction and crowding corrected surface number density (green) of stars in the magnitude ranges $9.75 - 17.75$ (left) and $14.75 - 17.75$ (right) and the corresponding light density (blue). The light density was derived from artificial images, taking into account only the fainter 80% of the pixel brightness distribution. The average light density was scaled to the average surface number density.

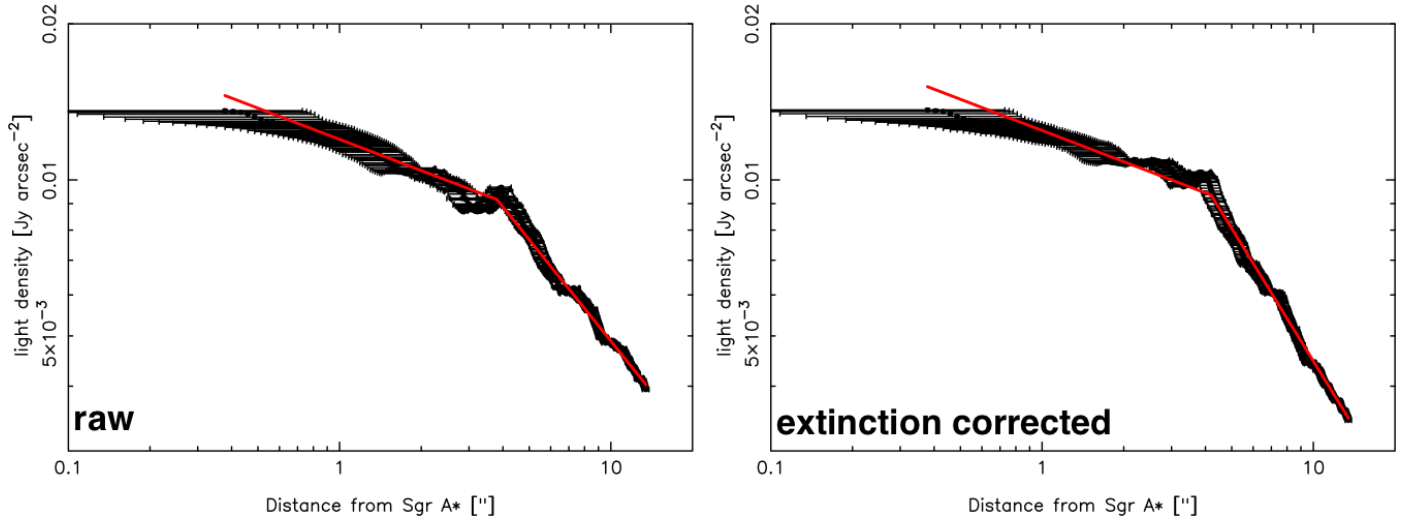


Fig. 14. Azimuthally averaged background light density extracted from the NACO AO data. The raw light density is shown in the left panel, while the background corrected light density is shown in the right panel (normalized to the raw counts). The straight red lines show a broken power law fit to the data. The parameters of the fit are $R_{\text{break}} = 4.0 \pm 0.8''$, $\Gamma_{\text{cusp}} = 0.15 \pm 0.07$, and $\Gamma_{\text{cluster}} = 0.85 \pm 0.07$ for the extinction corrected data (uncorrected: $R_{\text{break}} = 3.8 \pm 0.8''$, $\Gamma_{\text{cusp}} = 0.20 \pm 0.08$, $\Gamma_{\text{cluster}} = 0.65 \pm 0.10$).

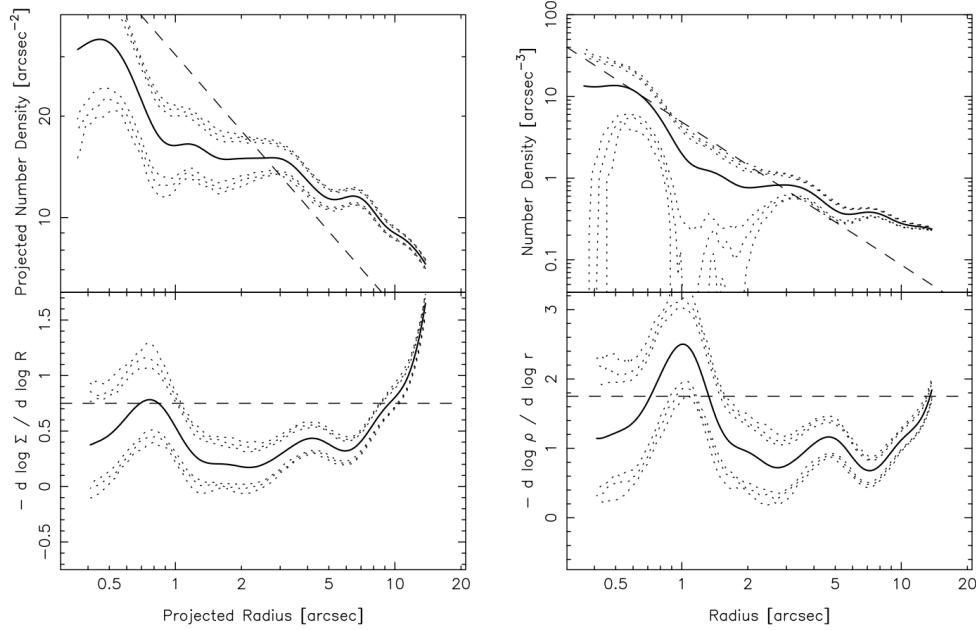


Fig. 15. The structure of the GC stellar cluster as derived from the NACO star counts ($9.75 \leq \text{mag}_K \leq 17.75$) with the nonparametric kernel estimator (see Merritt & Tremblay 1994), including all relevant corrections. Upper panel: Non-parametric kernel fit of the star counts. The dotted lines indicate the 90, 95, and 98% confidence limits from the bootstrap method described in (see Merritt & Tremblay 1994). The dashed line indicates the slope of a Bahcall-Wolf cusp (Bahcall & Wolf 1976, 1977), i.e. $\sigma \propto R^{-0.75}$ for the surface density and $\rho \propto r^{-1.75}$ for the space density, where R is the projected and r the 3D distance from Sgr A*. The lower panel shows a plot of the power-law slope of the stellar surface density vs. distance from Sgr A* as it results from the kernel fit. The dashed line indicates the slope of a single-mass Bahcall-Wolf cusp.

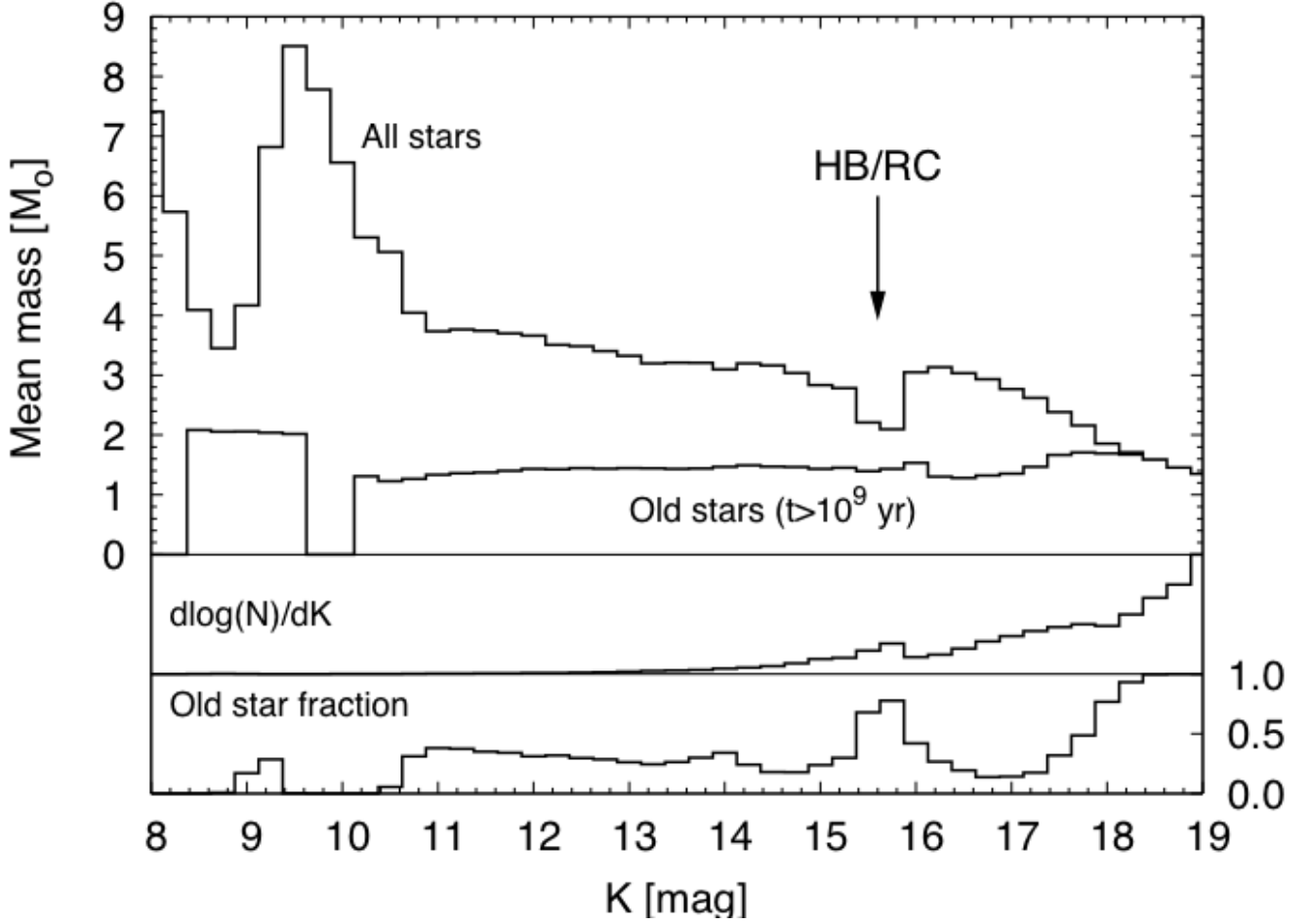


Fig. 16. The predicted mean stellar mass as function of K magnitude for the total population and for the old stars based on a population synthesis model for the central parsecs of the GC (Alexander & Sternberg (1999); Alexander (2005), based on the $Z = 1.5 Z_{\odot}$ stellar evolution tracks of Schaller et al. (1992) and Girardi et al. (2000)). The model assumes continuous star formation at a constant rate over the last 10 Gyr with a Miller-Scalo initial mass function (Miller & Scalo (1979)). A distance to the GC of 7.62 kpc and an extinction coefficient of $A_K = 2.8$ mag (Eisenhauer et al. 2005) are assumed. The relative number of old stars (defined here as stars with a lifespan longer than 10^9 yr) is shown in the bottom panel. The increase in the fraction of old stars to 0.8 at $K \sim 15.5$ mag, is matched by an abrupt decrease in the overall mean mass (top panel). This reflects the concentration of red clump / horizontal branch (HB/RC) giants at that magnitude, as seen in the K -band luminosity function (KLF) (middle panel). The dotted lines parallel to the x-axis, at y-values between 0 and 1, are merely an aid for analysing the plot.

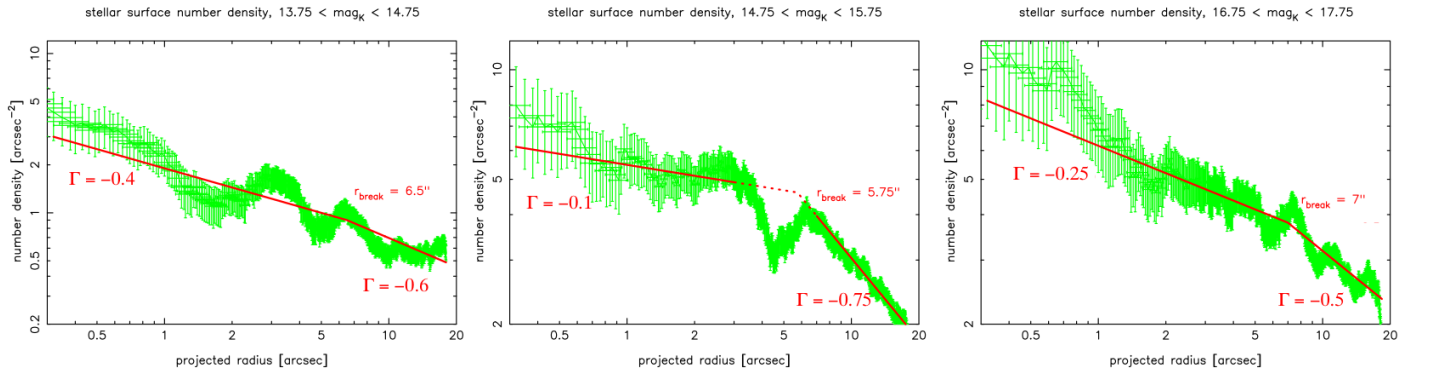


Fig. 17. Azimuthally averaged extinction and crowding corrected surface density vs. distance from Sgr A* for the K -magnitude ranges 13.75–14.75, 14.75–15.75, and 16.75–17.75. Broken power-law are fits are indicated by the red lines with the corresponding power-law indices indicated in the panels. A 1σ uncertainty of 0.05 can be assumed for all indices, and of $0.5''$ for the break radii. The data in the dip that can be seen in the middle panel around $5''$ were not included in the fitting process for the intermediate bright stars. This is indicated by the dashed line of the fitted broken power-law in the corresponding region.

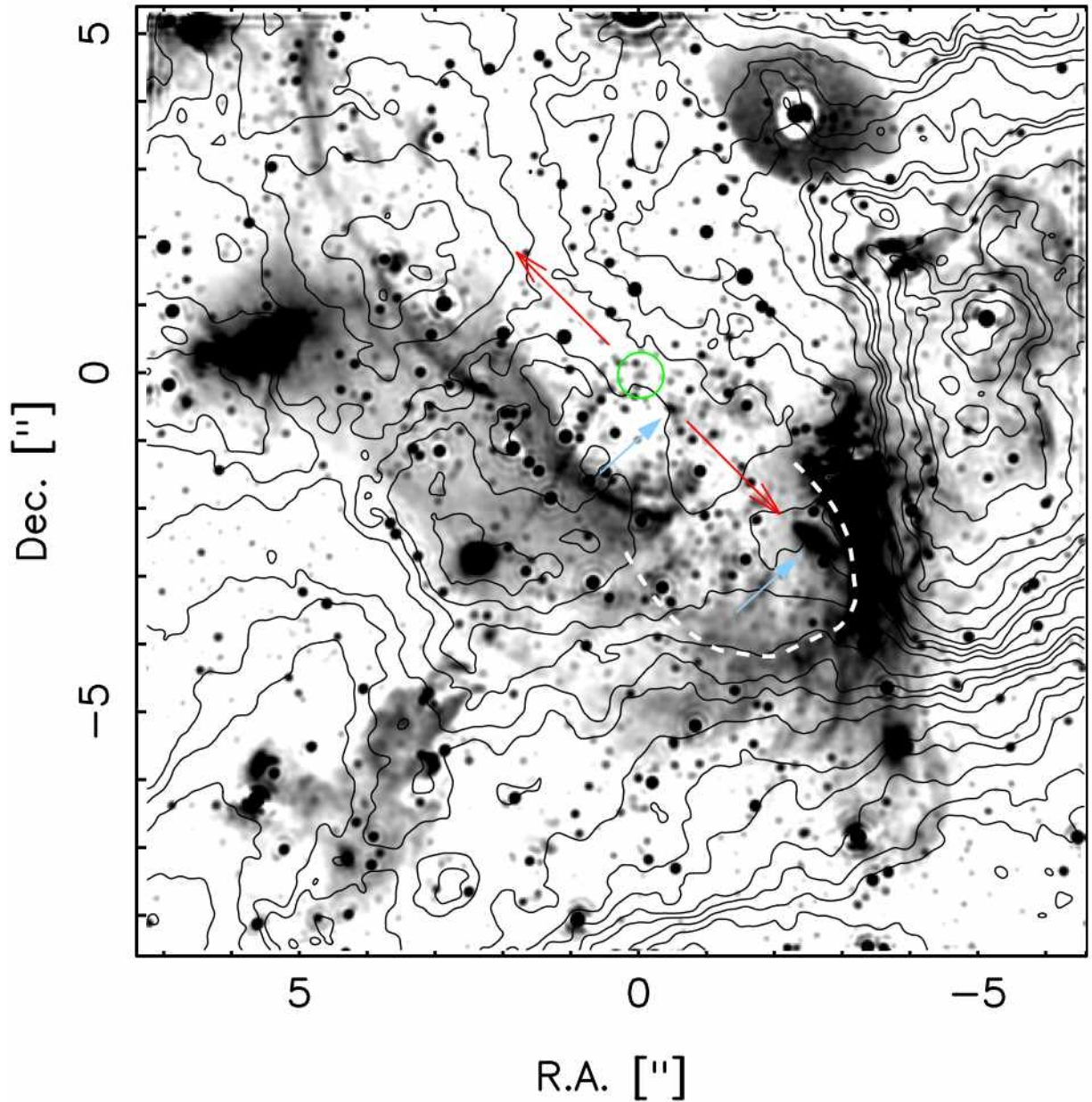


Fig. 18. Extinction contours (see Fig. 8) superposed onto a NACO L'-band image (July 2004; Lucy-Richardson deconvolved and restored with a Gaussian beam to a resolution of $\sim 0.1''$; logarithmic scaling) of the central $10'' \times 10''$ of the GC. The mini-cavity is marked. The arrows indicate the direction of a possible outflow from Sgr A*. Sgr A* is located at the origin of the coordinate system and is marked by a circle. It is visible as a faint point source (see Genzel et al. 2003a; Eckart et al. 2006a; Clénet et al. 2004; Ghez et al. 2004). The (red) arrows pointing into opposing directions away from Sgr A* indicate the direction of a possible outflow (see Mužić et al., in prep.). The white dashed line indicates the contours of the mini-cavity. The (blue) arrows (pointing up and towards the right) indicate cometary like features that may lie within the outflow, are pointed away from it and are aligned with the direction toward Sgr A*. The shock-like filaments may have been created by the outflow (possibly expanding laterally) as well (see Mužić et al., in prep.).

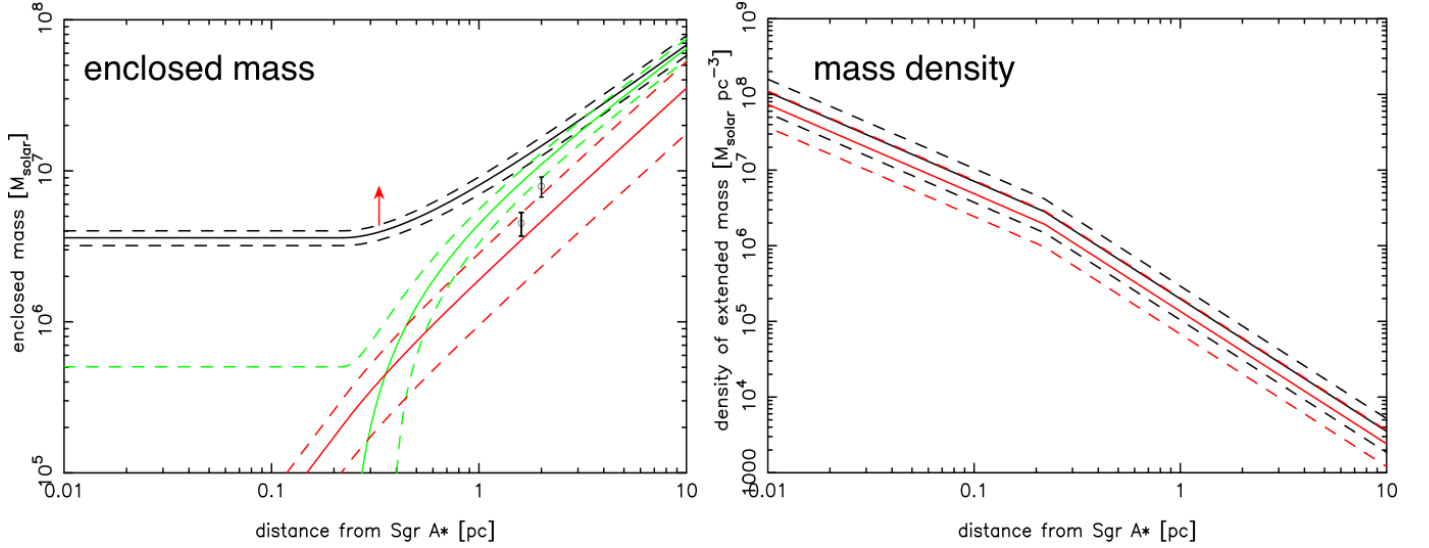


Fig. 19. Left panel: Black line: Estimate of the enclosed mass vs. projected distance, derived with the Bahcall-Tremaine (BT) mass estimator, assuming a broken power-law structure of the stellar cluster and a constant line-of-sight velocity dispersion outside of the break radius (see text for details). The up-pointing red arrow is the enclosed mass estimate based on IRS 9 (Reid et al., astro-ph/0612164). The circle at 1.6 pc is the mass estimate based on the assumption that the CND is a rotating ring with a rotation velocity of 110 km s^{-1} and a radius of 1.6 pc (Christopher et al. 2005). The circle at 2.0 pc is the mass estimate based on the assumption that the CND is a rotating ring with a rotation velocity of 130 km s^{-1} and a radius of 2.0 pc (Rieke & Rieke 1988; Guesten et al. 1987). The dashed lines indicate the 1σ uncertainties. Green line: enclosed mass after subtraction of the black hole mass, derived from the BT mass estimator (black). Red line: estimated mass of the visible stellar cluster. The dashed lines indicate the 1σ uncertainties. **Right panel:** Density of the enclosed mass, after subtraction of the black hole mass (black). The red line indicates the mass density of the stellar cluster. The dashed lines indicate the 1σ uncertainties.